Draft version February 6, 2020
Typeset using LaTeX **modern** style in AASTeX63

arXiv:2002.00014v2 [astro-ph.SR] 5 Feb 2020

Close Binary Companions to APOGEE DR16 Stars: 20 000 Binary-star Systems Across the Color–Magnitude Diagram

Adrian M. Price-Whelan,[1] David W. Hogg,[1,2,3] Hans-Walter Rix,[3] Rachael L. Beaton,[4,5,*] Hannah Lewis,[6] David L. Nidever,[7,8] Andrés Almeida,[9] Rodolfo Barba,[10] Timothy C. Beers,[11] Joleen K. Carlberg,[12] Nathan De Lee,[13,14] José G. Fernández-Trincado,[15] Peter M. Frinchaboy,[16] D. A. García-Hernández,[17,18] Paul J. Green,[19] Sten Hasselquist,[20,†] Penélope Longa-Peña,[21] Steven R. Majewski,[6] Christian Nitschelm,[21] Jennifer Sobeck,[22] Keivan G. Stassun,[14] Guy S. Stringfellow,[23] and Nicholas W. Troup[24]

[1] *Center for Computational Astrophysics, Flatiron Institute, Simons Foundation, 162 Fifth Avenue, New York, NY 10010, USA*

[2] *Center for Cosmology and Particle Physics, Department of Physics, New York University, 726 Broadway, New York, NY 10003, USA*

[3] *Max-Planck-Institut für Astronomie, Königstuhl 17, D-69117 Heidelberg, Germany*

[4] *Department of Astrophysical Sciences, Princeton University, 4 Ivy Lane, Princeton, NJ 08544*

[5] *The Observatories of the Carnegie Institution for Science, 813 Santa Barbara St., Pasadena, CA 91101*

[6] *Department of Astronomy, University of Virginia, Charlottesville, VA 22904-4325, USA*

[7] *Department of Physics, Montana State University, P.O. Box 173840, Bozeman, MT 59717-3840*

[8] *NSFs National Optical-Infrared Astronomy Research Laboratory, 950 North Cherry Ave, Tucson, AZ 85719*

[9] *Instituto de Investigación Multidisciplinario en Ciencia y Tecnología, Universidad de La Serena, Benavente 980, La Serena, Chile*

[10] *Departamento de Astronomía, Facultad de Ciencias, Universidad de La Serena, Cisternas 1200, La Serena, Chile*

[11] *Department of Physics and JINA Center for the Evolution of the Elements, University of Notre Dame, Notre Dame, IN 46556, USA*

[12] *Space Telescope Science Institute, 3700 San Martin Dr, Baltimore MD 21218*

[13] *Department of Physics, Geology, and Engineering Technology, Northern Kentucky University, Highland Heights, KY 41099*

[14] *Department of Physics and Astronomy, Vanderbilt University, VU Station 1807, Nashville, TN 37235, USA*

[15] *Instituto de Astronomía y Ciencias Planetarias, Universidad de Atacama, Copayapu 485, Copiapó, Chile*

[16] *Department of Physics & Astronomy, Texas Christian University, Fort Worth, TX, 76129, USA*

[17] *Instituto de Astrofísica de Canarias (IAC), E-38205 La Laguna, Tenerife, Spain*

[18] *Universidad de La Laguna (ULL), Departamento de Astrofísica, E-38206 La Laguna, Tenerife, Spain*

[19] *Center for Astrophysics — Harvard & Smithsonian, 60 Garden Street, Cambridge, MA 02138, USA*

[20] *Department of Physics and Astronomy, University of Utah, 115 S. 1400 E., Salt Lake City, UT 84112, USA*

[21] *Centro de Astronomía (CITEVA), Universidad de Antofagasta, Avenida Angamos 601, Antofagasta 1270300, Chile*

[22] *Department of Astronomy, University of Washington, Box 351580, Seattle, WA 98195, USA*

aprice-whelan@flatironinstitute.org

Corresponding author: Adrian M. Price-Whelan

[23] *Center for Astrophysics and Space Astronomy, Department of Astrophysical and Planetary Sciences, University of Colorado, 389 UCB,Boulder, CO 80309-0389, USA*
[24] *Department of Physics, Salisbury University, Salisbury, MD 21801*

ABSTRACT

Many problems in contemporary astrophysics—from understanding the formation of black holes to untangling the chemical evolution of galaxies—rely on knowledge about binary stars. This, in turn, depends on discovery and characterization of binary companions for large numbers of different kinds of stars in different chemical and dynamical environments. Current stellar spectroscopic surveys observe hundreds of thousands to millions of stars with (typically) few observational epochs, which allows binary discovery but makes orbital characterization challenging. We use a custom Monte Carlo sampler (*The Joker*) to perform discovery and characterization of binary systems through radial-velocities, in the regime of sparse, noisy, and poorly sampled multi-epoch data. We use it to generate posterior samplings in Keplerian parameters for 232 531 sources released in APOGEE Data Release 16. Our final catalog contains 19 635 high-confidence close-binary ($P \lesssim$ few years, $a \lesssim$ few AU) systems that show interesting relationships between binary occurrence rate and location in the color–magnitude diagram. We find notable faint companions at high masses (black-hole candidates), at low masses (substellar candidates), and at very close separations (mass-transfer candidates). We also use the posterior samplings in a (toy) hierarchical inference to measure the long-period binary-star eccentricity distribution. We release the full set of posterior samplings for the entire parent sample of 232 531 stars. This set of samplings involves no heuristic "discovery" threshold and therefore can be used for myriad statistical purposes, including hierarchical inferences about binary-star populations and sub-threshold searches.

* Hubble Fellow
Carnegie-Princeton Fellow
† NSF Astronomy and Astrophysics Postdoctoral Fellow

1. INTRODUCTION

Binary star systems provide key context and constraints for nearly all subfields in astrophysics (e.g., Price-Whelan et al. 2019; Rix et al. 2019). For two concrete examples, a measurement of the occurrence rate of stellar-mass black holes in the Milky Way would enable new constraints on binary black hole formation channels to explain merger events observed by LIGO (Abbott et al. 2016, 2019), and interpretation of spectroscopic observations of high-redshift galaxies and their stellar populations depends on understanding the impacts of binary star evolution on stellar population parameters (e.g., Eldridge et al. 2017). One common need for all applications is improved constraints on the population properties (e.g., period, eccentricity, and mass ratio distributions, occurrence rates) of stellar multiplets and their variations with stellar type, chemistry, and dynamical environment, especially at the extrema of these stellar characteristics. This has only been comprehensively done for a sample of a few hundred stars in solar neighborhood (Raghavan et al. 2010), for specific stellar types (e.g., Moe & Di Stefano 2017), or with imprecise statistics using large samples of stars (Badenes et al. 2018).

While this problem spans a huge range in timescales (from hours to millenia), current or near-future stellar surveys (e.g., *Gaia*, APOGEE, LAMOST, SDSS-V; Gaia Collaboration et al. 2016, 2018; Majewski et al. 2017; Zhao et al. 2012; Kollmeier et al. 2017) have the capacity to deliver samples of binary stars and stellar companions orders of magnitude larger than are presently known, throughout all stages of stellar evolution. Even with existing datasets, we now have large enough sample sizes and the robust tools needed to perform hierarchical inferences to constrain much more detailed models of binary star formation and evolution (e.g., Moe & Kratter 2018; El-Badry & Rix 2019). However, the most precise measurements of the binary star population properties will benefit from joint analysis of all stellar surveys, which cover a range of stellar types, wavelengths, and measurement techniques.

As a step towards large-scale population inference, we focus here on multi-epoch spectroscopic data from the APOGEE surveys. This survey sequence has predominantly targeted red-giant stars (although with DR16 there are now many main-sequence stars, see below). Because of operational re-visit decisions to reach signal-to-noise thresholds, the surveys deliver some time-domain information, although they were not designed with binary-star characterization as highest priority. The fundamental data are $R \sim 20\,000$ H-band spectroscopy taken with the primary purpose of mapping the Milky Way in elemental abundances and kinematics. This survey is not the perfect target for binary-star identification, but it arguably has one of the best combinations of spatial reach around the Milky Way, coverage of the color-magnitude diagram, and multi-epoch data.

The challenge of working with data that were *not* taken primarily for binary characterization is that the data are sparse, time baselines are variable, and most individual systems are not characterized uniquely (in orbital parameters). Indeed, period-fitting tasks generically produce multi-modal likelihood functions and posterior pdfs for periods, amplitudes, and phases, and the Kepler problem is no different. These

multi-modal likelihood functions are a nightmare for optimization or sampling. For this reason we created a custom sampler *The Joker* (Price-Whelan et al. 2017) that performs brute-force rejection sampling using a large, initial prior sampling. Because this sampler does not produce Markov Chains, but rather just uses dense prior samples, it does not get "stuck" in local optima; It samples the full parameter space, with zero autocorrelation among samples. To proceed, however, the sampler makes strong assumptions, that the source is a single-lined spectroscopic binary (SB1) with only one companion (for example). But it generates full samplings over orbital parameters for arbitrarily sampled radial-velocity data.

Importantly, we use *The Joker* to sample *every* APOGEE target as if it were an SB1 (see Section 7 for some discussion of the implications of this assumption). Discovery of which stars really do have companions then becomes a post-processing step on the confidence of the characterization: This project deliberately conflates discovery with characterization. This has the added advantage that we deliver full posterior samplings even for stars that aren't obviously in binary systems; these can be used for statistical studies and sub-threshold searches when new data arrive (i.e., future surveys or follow-up). In what follows, we run *The Joker* on all of APOGEE DR16 (subject to some quality cuts) and release the resulting catalog of posterior samples, along with some summary metadata for the subsample with good, uniquely determined companions and orbits. We demonstrate the use of the samplings with a few examples of interesting objects and a simple hierarchical probabilistic populations inference.

This *Article* is similar to Price-Whelan et al. (2018) but should be viewed as a strict replacement (rather than an improvement) of the catalogs and results of that work: We have made substantial improvements to the methodology (improvements to *The Joker*, see Appendix A), and the APOGEE data in DR16 are of higher quality, substantially larger in volume, and have more observation epochs.

2. DATA

We use spectroscopic data from data release 16 (DR16) of the APOGEE surveys (Majewski et al. 2017; Ahumada et al. 2019; Jönsson et al., in prep.). APOGEE is a component of the Sloan Digital Sky Survey IV (SDSS-IV; Gunn et al. 2006; Blanton et al. 2017) and its main goal is to survey the chemical and dynamical properties of stars across much of the Milky Way disk by obtaining high-resolution ($R \sim 22,500$; Wilson et al. 2019) infrared (H-band) spectroscopy of hundreds of thousands of stars. The primary survey targets are selected with simple color and magnitude cuts (Zasowski et al. 2013, 2017), but the survey uses fiber-plugged plates that cover only a small fraction of the by area, which leads to extremely nonuniform coverage of the Galactic stellar distribution (see, e.g., Figure 1 in Ahumada et al. 2019).

DR16 is the first SDSS data release to contain APOGEE data observed with a duplicate of the APOGEE spectrograph on the 2.5m Irénée du Pont telescope (Bowen & Vaughan 1973) at Las Campanas Observatory, providing access to targets in the southern hemisphere. For the first time, this data release also contains calibrated stellar parameters for dwarf stars (Jönsson et al., in prep.). These two facts mean that

DR16 contains nearly 3 times more sources with calibrated stellar parameters than the previous public data release, DR14 (Abolfathi et al. 2017; Holtzman et al. 2018; see Section 4 of Ahumada et al. 2019 for many more details about APOGEE DR16).

Most APOGEE stars are observed multiple times in separate "visits" that are combined before the APOGEE data reduction pipeline (Nidever et al. 2015; Zamora et al. 2015; García Pérez et al. 2016) determines stellar parameters and chemical abundances for each source. While the visit spectra naturally provide time-domain velocity information about sources (thus enabling searches for massive companions), studying stellar multiplicity is not the primary goal of the survey: The cadence and time baseline for a typical APOGEE source is primarily governed by trying to schedule a set number of visits determined by signal-to-noise thresholds for the faintest targets in a given field. A small number of fields (five) were designed specifically for companion studies and have > 10 visits spaced to enable binary system characterization.

While some past studies have made use of other fields with large numbers of visits to study binary-star systems (Troup et al. 2016; Fernández-Trincado et al. 2019), a consequence of this strategy is that the time resolution and number of visits for the vast majority of APOGEE sources in DR16 is not sufficient for fully determining companion orbital properties, as illustrated below. Still, the large number of targets in APOGEE and the dynamic range in stellar and chemical properties offers an exciting opportunity to study the *population* of binary star systems as a function of these intrinsic properties, even if most individual systems are poorly constrained. We have previously developed tools to enable such studies (Price-Whelan et al. 2017), as summarized in Section 3 below. Here, we describe quality cuts we apply to the APOGEE DR16 catalogs before proceeding, and modifications to the visit-level velocity uncertainties to account for the fact that they are generally underestimated by the APOGEE data reduction pipeline.

2.1. *Quality cuts and defining a parent sample*

The primary goal of this *Article* is to produce a catalog of posterior samplings in Keplerian orbital parameters for *all* high-quality APOGEE sources in DR16 with multiple, well-measured radial velocities. We therefore impose a set of quality cuts to sub-select APOGEE DR16 sources by rejecting sources or visits using the following APOGEE bitmasks (Holtzman et al. 2018, Jönsson et al., in prep.):

- Source-level (`allStar`) `STARFLAG` must not contain `VERY_BRIGHT_NEIGHBOR`, `SUSPECT_RV_COMBINATION` (bitmask values: 3, 16)
- Source-level (`allStar`) `ASPCAPFLAG` must not contain `TEFF_BAD`, `LOGG_BAD`, `VMICRO_BAD`, `ROTATION_BAD`, `VSINI_BAD` (bitmask value: 16, 17, 18, 26, 30)
- Visit-level (`allVisit`) `STARFLAG` must not contain `VERY_BRIGHT_NEIGHBOR`, `SUSPECT_RV_COMBINATION`, `LOW_SNR`, `PERSIST_HIGH`, `PERSIST_JUMP_POS`, `PERSIST_JUMP_NEG` (bitmask value: 3, 9, 12, 13, 16)

These bitmasks are designed to remove the most obvious data reduction or calibration failures that would directly impact the visit-level radial velocity determinations.

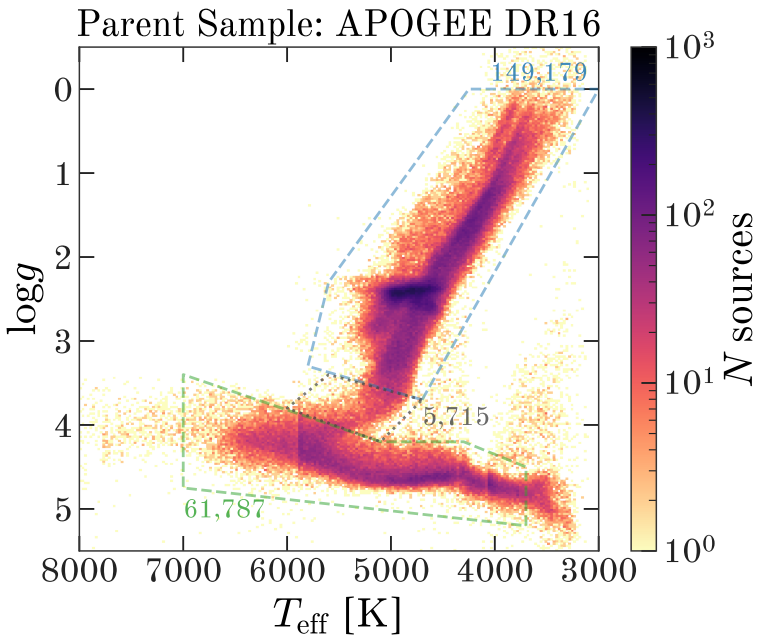

Figure 1. Two spectroscopic (ASPCAP) stellar parameters—effective temperature, $T_{\rm eff}$, and log-surface gravity, $\log g$—of APOGEE DR16 sources that pass our quality cuts. These sources represent our "parent sample." The pixel coloring indicates the number of sources in each bin of stellar parameters. The outlined regions roughly identify the red giant branch (upper polygon, blue), subgiant branch (middle polygon, black), and (FGK-type) main sequence (lower polygon, green). The numbers next to each selection polygon indicate the number of sources in each.

However, we later impose a stricter set of quality masks when showing results in Section 6.2. After applying the above masks, we additionally reject any source with < 3 visits. Our final parent sample contains 232 531 unique sources, selected from the 437, 485 unique sources in all of APOGEE DR16. Of the ≈200, 000 sources removed, the vast majority were dropped because they had < 3 visits (≈17 000 were removed by the quality cuts).

Figure 1 shows the sources in our parent sample—i.e. APOGEE sources with 3 or more visits that pass the quality cuts described above—as a function of spectroscopic stellar parameters $T_{\rm eff}$, effective temperature, and $\log g$, log-surface gravity. While the majority of sources are giant-branch stars ($> 150\,000$), a substantial number of main sequence stars are present ($> 60\,000$) thanks to the APOGEE data reduction pipeline improvements for DR16 (Jönsson et al., in prep.). Figure 2 shows some statistics about the time coverage of the visits for sources in our parent sample. About half of the sources have a small number of visits spread over a small time baseline (the time spanned from the first to last visit for each source): 50% of sources have < 5 visits over < 100 days. About 7% of sources (15 366) have ≥ 10 visits over ≥ 100 days.

2.2. *Visit velocity uncertainty calibration*

The significance of apparent radial velocity variations, especially when considering low-mass or long-period companions, will depend strongly on the accuracy of the visit

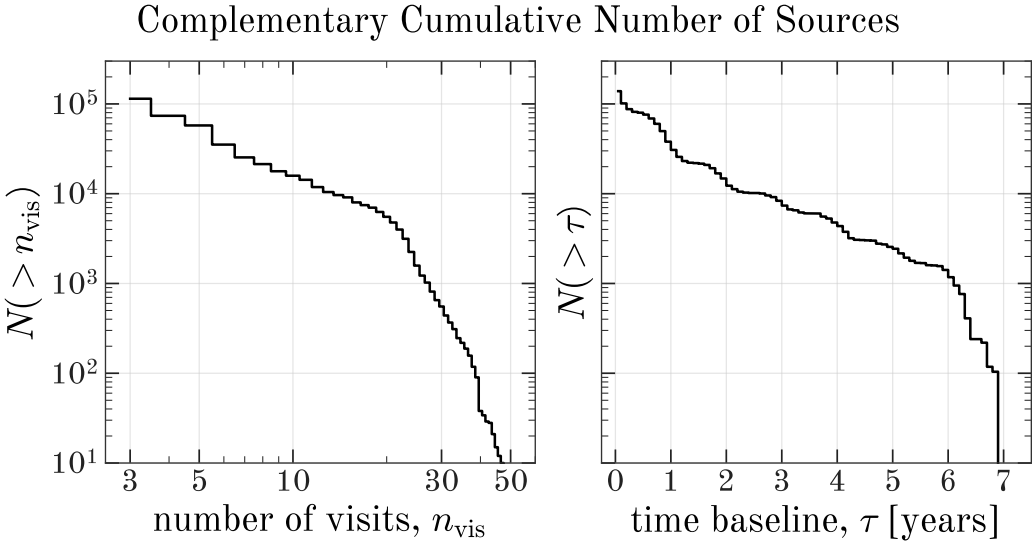

Figure 2. Some statistics of APOGEE DR16 visits. **Left:** The number of sources with more than a given number of visits, $n_{\rm vis}$. While ≈50% of sources have 3 visits, (114 263, 57 593, 15 862) sources have $>(3, 5, 10)$ visits, respectively. A very small number of sources have >50 visits. **Right:** The number of sources with a time baseline, τ, longer than given (on the horizontal axis). While ≈50% of sources have a time baseline $\tau \lesssim 56$ day, (88 737, 9 743) sources have $\tau > (100, 1\,000)$ days.

velocity measurement errors. However, the catalog-level APOGEE visit velocity errors (`VRELERR` in the `allVisit` file) are known to be underestimated (e.g., Cottaar et al. 2014). Here, we adopt the relation defined in Brown et al. (in prep.) to scale up the visit velocity errors

$$\sigma_v^2 = (3.5\,(\texttt{VRELERR})^{1.2})^2 + (0.072\ \mathrm{km\ s^{-1}})^2 \quad (1)$$

where σ_v is the adopted visit velocity error for a given visit, and `VRELERR` is the uncertainty reported in the APOGEE DR16 catalog. This effectively applies a floor to the visit velocity errors of 72 m s^{-1} and globally increases the error values by a multiplicative factor.

3. METHODS

As illustrated above, a large number of sources in APOGEE DR16 have few visits that span a short time baseline. For most sources, we therefore expect that even if visit-level radial velocity variations are detected with high significance, the companion orbital parameters will be very uncertain—i.e. the posterior probability distribution function (*pdf*) over orbital parameters will generally be multi-modal with many modes of comparable integrated probability (e.g., Price-Whelan et al. 2017). Still, in unison, or within the context of a hierarchical model that utilizes the individual posterior samplings, the combination of all of these individually weakly-constrained binary star orbits provides information about the population of binary stars. We have previously defined and implemented a custom Monte Carlo sampler for precisely this problem: *The Joker* (Price-Whelan et al. 2017). *The Joker* is designed to deliver converged posterior samplings over Keplerian orbital parameters given radial velocity

observations, even when the observations are sparse or very noisy. Its prior application to APOGEE DR14 (Price-Whelan et al. 2018) resulted in a released catalog of over $5,000$ binary star systems; this *Article* and companion catalog is a successor to this previous work.

As before, we use a parametrization of the two-body problem in which the radial velocity, v, of an observed star in a binary system (referred to as the *primary*, even if it is less massive than its companion) can be expressed as:

$$v(t) = K\,\zeta(t\,;\,P, e, \omega, M_0, t_0) + v_0 \tag{2}$$

where K and v_0 are linear parameters (in time t). The other parameters—period P, eccentricity e, argument of periastron ω, reference time t_0, and mean anomaly at reference time M_0—enter through the nonlinear function

$$\zeta(t\,;\,P, e, \omega, M_0, t_0) = \cos\left(f + \omega\right) + e\,\cos\omega \tag{3}$$

where f is the true anomaly, and we always set the reference time, t_0, to the minimum observation time for a given set of radial velocity observations.

3.1. *Updates to The Joker*

Since our initial paper defining *The Joker*, we identified a conceptual error in the assumptions made about the prior over the linear parameters (K, v_0) in Price-Whelan et al. (2017). We previously assumed that adopting a sufficiently broad, Gaussian prior over the linear parameters meant that we could ignore an explicit definition of this prior. In particular, this allowed us to drop any terms related to the prior over these parameters in the marginal likelihood expression (Equation 11 in Price-Whelan et al. 2017). This assumption is not correct, and can lead to unexpected behavior when applied to data that are very noisy or have a small time baseline compared to the samples of interest. We have rewritten the expression for the marginal likelihood that underlies *The Joker* in Appendix A, based on the notation in Hogg et al. (in prep.).

Another issue with the assumption in the original implementation of *The Joker* is that the prior over the velocity semi-amplitude, K, was identical at all period and eccentricity values. This implies vastly different prior beliefs about the companion mass as a function of orbital period: For example, a zero-mean Gaussian prior on K with a standard-deviation of 30 km s^{-1} transforms to reasonable prior beliefs about companion mass at periods around 1 yr, but gives substantial prior probability to companion masses > 100 M$_\odot$ at periods $> 10^4$ d. We therefore, by default, adopt a new (also Gaussian) prior on the semi-amplitude with a variance, σ_K^2, that scales with the period and eccentricity such that

$$\sigma_K^2 = \sigma_{K,0}^2 \left(\frac{P}{P_0}\right)^{-2/3} \left(1 - e^2\right)^{-1} \tag{4}$$

where $\sigma_{K,0}$ and P_0 are additional hyperparameters that must be specified. This new prior on K has the advantage that it, at fixed primary mass, has a fixed form in companion mass that does not depend on period or eccentricity.

parameter	prior	description
nonlinear parameters		
P	$\ln P \sim \mathcal{U}(2, 16384)$ day	period
e	$e \sim \mathrm{Beta}(0.867, 3.03)$	eccentricity
t_0	fixed (minimum time)	reference time
M_0	$M_0 \sim \mathcal{U}(0, 2\pi)$ rad	mean anomaly at reference time
ω	$\omega \sim \mathcal{U}(0, 2\pi)$ rad	argument of pericenter
s	$\ln s \sim \mathcal{N}(\mu_y, \sigma_y^2)$	extra "jitter" added in quadrature to each visit velocity error
linear parameters		
K	$K \sim \mathcal{N}(0, \sigma_K^2)$ km s^{-1}	velocity semi-amplitude, where σ_K is given by Equation 4
	$\sigma_{K,0} = 30$ km s^{-1}	(see Equation 4)
	$P_0 = 365$ d	(see Equation 4)
v_0	$v_0 \sim \mathcal{N}(0, \sigma_{v_0}^2)$ km s^{-1}	system barycentric velocity
	$\sigma_{v_0} = 100$ km s^{-1}	

Table 1. Summary and description of parameters and prior *pdf*s. Beta(a, b) is the beta distribution with shape parameters (a, b), $\mathcal{U}(a, b)$ the uniform distribution over the domain (a, b), and $\mathcal{N}(\mu, \sigma^2)$ is the normal distribution with mean μ and variance σ^2.

We have also made a number of improvements to the Python implementation of the sampler.[1] For example, the prior distributions over all parameters are now specified as `pymc3` (Salvatier et al. 2016) distribution objects, meaning that the priors over the nonlinear Keplerian parameters (P, e, ω, and M_0; see Price-Whelan et al. 2017) are now fully customizable. Using `pymc3` also enables compatibility with more efficient Markov Chain Monte Carlo methods such as Hamiltonian Monte Carlo (HMC), which is useful for seamlessly transitioning from generating posterior orbit samples with *The Joker* to HMC when the system parameters are highly constrained (as discussed below).

4. RUNNING *The Joker* ON APOGEE DR16

For each of the 232 531 sources in the parent catalog of sources selected from APOGEE DR16 (Section 2), we run *The Joker* (Price-Whelan et al. 2017) generate posterior samplings over the Keplerian orbital parameters, including an additional per-source uncertainty or "jitter" parameter that is added in quadrature to the (adjusted) APOGEE visit velocity uncertainties (see above). We start by generating a cache of $100,000,000$ prior samples for the nonlinear parameters generated from the prior *pdf* summarized in Table 1 (top rows). For each source, we iteratively read random blocks of samples out of this cache, evaluate the marginal likelihood, and rejection sample to produce posterior samplings in the nonlinear parameters. We repeat this iterative process until we reach the total number of samples in the cache, or until we obtain a requested number of prior samples, M_{min}; this is an arbitrary parameter that we set to

[1] https://github.com/adrn/thejoker

$M_{\rm min} = 512$ for this work. In practice, this is done by parallelizing the sampling (over sources) and takes about 8 hours to run on 720 cores on our local compute cluster (at the Flatiron Institute) for the entire sample.

After this procedure, the sources are in one of two stages of completion: Sources either have $M_{\rm min} = 512$ posterior samples (227 999 sources) and are complete, or $M_{\rm min} < 512$ posterior samples (4 496 sources) and more samples are needed. For sources that require more samples, these can be split again into two classes: Sources with unimodal samplings in period, and sources with multi-modal samplings (following the criteria described in Price-Whelan et al. 2017). For incomplete sources with multi-modal samplings (2 787 sources), these would need to be re-run with a much larger number of prior samples to reach 512 posterior samples, but here we mark these sources as incomplete. For incomplete sources with unimodal samplings (1 709 sources), we use the samples returned from *The Joker* to initialize Hamiltonian Monte Carlo (HMC) to continue generating posterior samples. We use `pymc3` with the *No-U-Turn Sampler* (NUTS; Homan & Gelman 2014), using the dense mass matrix tuning prescription implemented in `exoplanet` (Foreman-Mackey et al. 2019) and run 4 chains in parallel, each for 1000 tuning steps and 4000 steps subsequently. We use these 4 chains and `pymc3` to compute the Gelman-Rubin convergence statistic, $\hat{R}$ (Gelman & Rubin 1992), for each parameter for each source; If $\hat{R} < 1.1$ for all parameters, we down-sample to 512 samples and mark that source as MCMC-completed. If the HMC sampling fails (e.g., chains diverge substantially), we fall back to the sampling from *The Joker*—this generally only happens for data with serious systematic issues (e.g., one outlier visit velocity with an unreasonable velocity measurement).

At this point, we now have up to 512 posterior samples of the parameters listed in Table 1 for most of the 232 531 APOGEE sources in the parent sample. These full samplings will be released as a Value-Added Catalog (VAC) with the SDSS DR16+ "mini" data release planned for July 2020.

5. A CATALOG OF BINARY STARS

For some science cases and exploration, it is useful to define catalogs of systems with likely companions from the posterior samplings generated here, as we illustrate below. This requires making decisions and imposing hard cuts on the samplings returned by the above procedure. However, most of the orbital parameter samplings for most sources are highly uncertain and multi-modal, and it is therefore not possible to define simple cuts on physical parameters (e.g., companion mass) to produce a simple catalog. In the previous iteration of this work (Price-Whelan et al. 2018), we defined cuts based on percentiles computed from the distribution of $\ln K$ values after comparing to running the same pipeline on a control sample of data generated with purely Gaussian noise properties and time information taken from the APOGEE DR14 visits. Here, we use both a selection based on the posterior samples in K and based on a likelihood ratio comparing the Keplerian orbit model assumed by *The Joker* with a (robust) constant-velocity model for each source.

Following Price-Whelan et al. (2018), we again compute the 1st-percentile values of the posterior samples in $\ln K$ for each source and refer to these values as $P_{1\%}(\ln K)$; this amounts to an estimate of the 99% confidence lower-limit on the (log) velocity semi-amplitude. We again also generate a simulated control sample of data to assess contamination when making selections using this quantity. For each APOGEE source in our parent sample, we take the maximum *a posteriori* sample returned from the procedure defined above and subtract the orbit computed from this sample from the visit velocity data. We then re-run *The Joker* on all of the residual data, and compute $P_{1\%}(\ln K)$ for each star in the control sample. We find that $< 5\%$ of the control sample pass a cut of $P_{1\%}(\ln K) > 0$ (i.e., a conservative cut to require that sources have a velocity semi-amplitude > 1 km s^{-1}).

For each APOGEE source, after generating the posterior samplings, we compute and store the maximum (over posterior samples) *unmarginalized* log-likelihood value for the Keplerian orbit model, i.e., for one source with N visit velocity measurements v_n at times t_n,

$$\ln \hat{L}_1 = \sum_n^N \ln \mathcal{N}(v_n \,|\, v(t_n\,;\, \boldsymbol{\theta}_{\max}), \sigma_n^2) \tag{5}$$

where σ_n are the adjusted visit velocity errors (Equation 1) and $v(\cdot)$ is given by Equation 2 and is evaluated using the parameters for the maximum likelihood posterior sample, $\boldsymbol{\theta}_{\max}$.

For each source, we then also compute the maximum log-likelihood value for the visit data under a model that assumes that the visit velocities are drawn from a constant velocity with Gaussian uncertainties but allowing for $< 20\%$ outliers; we refer to this model as a *robust constant-velocity* model for the visit velocities. Using the same notation for the visit velocity data as above, the likelihood under this model is given by

$$\hat{L}_2 = \prod_n^N \left[(1-f)\,\mathcal{N}(v_n \,|\, \mu_v, \sigma_n^2) + f\,\mathcal{N}(v_n \,|\, \mu_v, \sigma_n^2 + \Sigma)\right] \tag{6}$$

where f is the outlier fraction, μ_v is the constant-velocity value, and Σ is the variance of the outlier model component (assumed to be large). We optimize this likelihood using the BFGS algorithm (Nocedal & Wright 2006) with bounds on the parameters such that $f \in (0, 0.2)$, $\mu_v \in (-500, 500)$ km s^{-1}, and $\Sigma \in (0, 3000)$ (km s^{-1})^2. We store the optimized log-likehihood value of the robust constant-velocity model and refer to this as $\ln \hat{L}_2$

We define a catalog of binary star systems based on the posterior samplings generated from *The Joker* by selecting sources for which

$$P_{1\%}(\ln K) > 0 \tag{7}$$

$$(\ln \hat{L}_1 - \ln \hat{L}_2) > 4.6 \quad . \tag{8}$$

The cut on the log-likelihood ratio comes from the (adopted) condition that the maximum Kepler model likelihood should be > 100 times the maximum robust

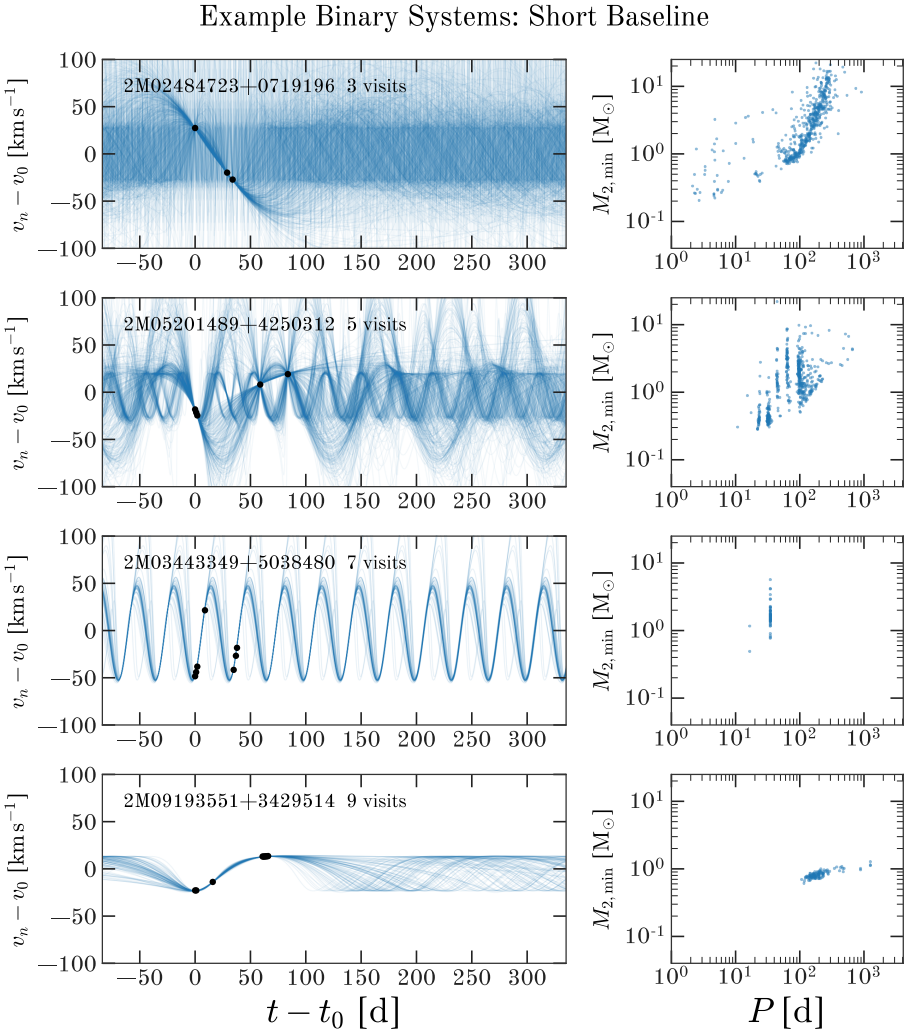

Figure 3. Example binary star systems that pass the selection and are included in the catalog released here for APOGEE sources with short visit baselines ($\tau < 100$ d). Each row is an APOGEE source (indicated on the left panel). Left panels show the visit velocity data (black markers; error bars are typically smaller than the marker) and radial velocity orbits computed from the posterior samples (blue lines). Right panels show the same samples in period P and minimum companion mass $M_{2,\mathrm{min}}$.

constant-velocity likelihood value. Of the 232 531 total sources in our parent sample, 19 635 sources pass the selection above; those are binary systems where we can provide meaningful orbit parameter samplings. Summary information for the samplings generated from all sources in the parent sample is included in Table 2; in this table, the boolean mask `binary_catalog` can be used to select the 19 635 sources that pass the binary star selections defined in Equation 8.

Figures 3 and 4 show some examples of binary systems that passed the selection above. In each figure, each row is a different APOGEE source, the two figures show some example short baseline (Figure 3) and long baseline (Figure 4) cases. The left column of panels in each figure show the radial velocity data (black markers) for randomly-chosen sources with (3, 5, 7, 9) visits (from top to bottom), and the blue lines show radial velocity orbits computed from the posterior samplings generated by

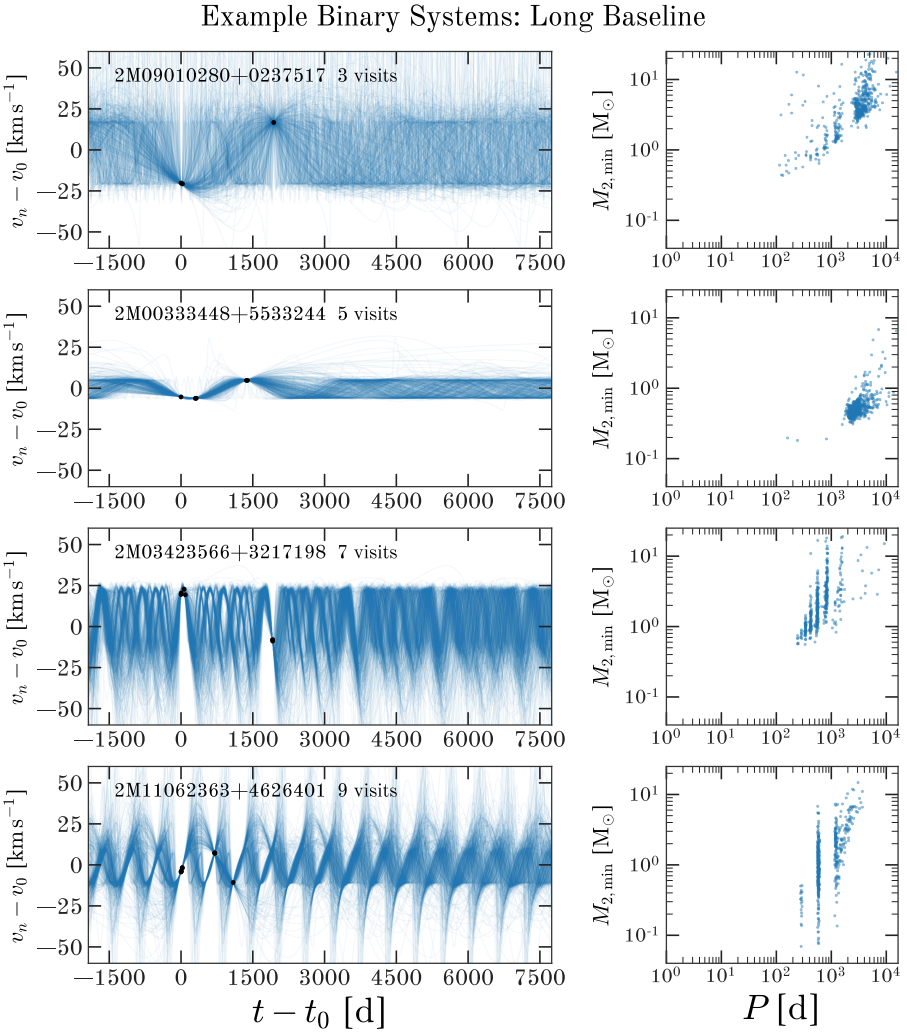

Figure 4. The same as Figure 3, but for APOGEE sources with long visit baselines ($\tau > 1000$ d)

The Joker. The right column of panels show the same posterior samples (blue markers), but in a projection of the parameter space (period P and minimum companion mass, $M_{2,\min}$). To compute $M_{2,\min}$, we use the posterior samplings from *The Joker* along with primary stellar masses computed by Queiroz et al. (2019) by sampling over the reported uncertainties on prior mass (assuming a Gaussian noise distribution on primary mass).

5.1. *The Gold Sample*

The majority of binary star systems that comprise the catalog defined above have strongly multi-modal samplings in orbital properties. While this is useful for binary *population* studies, it is more difficult to summarize the system orbital properties and their trends with stellar properties as it is not possible to simply compress the samplings. We therefore construct an additional catalog for the subset of sources that pass a more stringent set of quality cuts and have converged, unimodal or bimodal

posterior samplings. We define this *Gold Sample* as sources that pass the following cuts:

- Matches to a *Gaia* source within 2 arcsec of the reported 2MASS sky position,
- Has a stellar mass measurement in the STARHORSE catalog (Queiroz et al. 2019),
- No additional *Gaia* sources within 2 arcsec with a G-band magnitude difference $\Delta G > -5$ (to remove sources that would lie within the APOGEE fiber and appreciably contaminate the spectrum),
- No additional *Gaia* sources within 10 arcsec with a G-band magnitude difference $\Delta G > 2.5$ (to remove bright neighbor stars),
- $-0.5 < \log g < 5.5$ (reasonable stellar parameters),
- $3500 < T_{\rm eff} < 8000$ (reasonable stellar parameters),
- $-2.5 < [{\rm M/H}] < 0.5$ (reasonable stellar parameters),
- $s_{\rm MAP} < 0.5$ km s^{-1} (a small inferred excess variance),
- $n_{\rm vis} > 5$ (more than 5 visit spectra).

We identify sources with unimodal posterior samplings as sources for which the MCMC procedure succeeded (see Section 3). We identify sources with bimodal samplings using the same procedure as Price-Whelan et al. (2018). Briefly, we use a k-means clustering algorithm with $k = 2$ to identify clusters of samples in orbital period, and assess whether the samplings in each cluster are unimodal by checking whether all samples in each cluster lie within the mode size defined in Price-Whelan et al. (2017). In total, the *Gold Sample* contains 1 032 systems with unimodal samplings, and 492 systems with bimodal samplings. Summary information and a list of sources in the *Gold Sample* are included in Table 3.

6. RESULTS

The epoch baselines for most APOGEE sources, $\tau \lesssim 1$ yr, imply that most of the $\sim 20\,000$ binary systems (and certainly the $\sim 1\,000$ gold sample systems) will have $P \lesssim$ years and $a \lesssim$ few AU. However, the overall binary-star population extends from close binaries to systems with $a \gtrsim 20\,000$ AU, with a broad, approximately log-normal period distribution centered at $\sim \log(250$ yr) (Raghavan et al. 2010). The binary systems we identified and study here are commonly referred to as "close binaries" (Moe & Kratter 2018; Badenes et al. 2018), representing the closest $\sim 20\%$–40% of all bound binary star systems. With this in mind, we use our sample to study some simply population properties of these binary systems, and highlight some interesting systems in our sample.

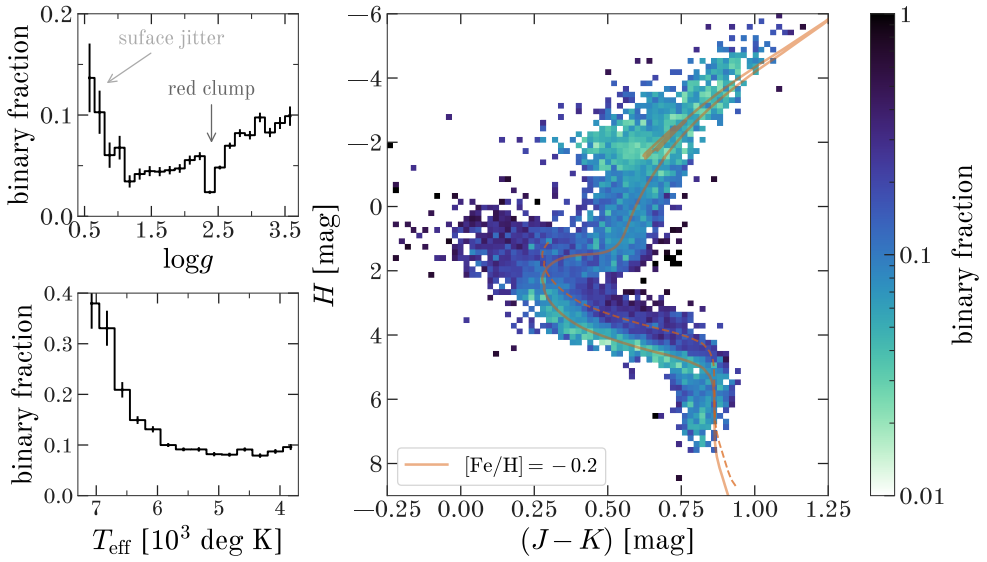

Figure 5. Close binarity across the color–magnitude diagram. **Upper left:** The observed close binary fraction as a function of spectroscopic surface gravity, $\log g$, for all stars that pass the giant branch selection indicated in Figure 1. **Lower left:** The observed binary fraction as a function of spectroscopic effective temperature, $T_{\rm eff}$, for all stars that pass the main sequence selection indicated in Figure 1. **Right:** The extinction-corrected 2MASS color-magnitude diagram (CMD) for all APOGEE sources, colored by the fraction of sources identified as binary-star systems (Section 5). The solid (orange) line shows a MIST isochrone for a 5 Gyr stellar population with [Fe/H] = −0.2, and the dashed line indicates the corresponding equal-mass binary sequence for main sequence stars. The panels in this figure are meant to be illustrative and should only be compared in a relative sense.

6.1. *Close binary fraction trends with stellar properties*

Our catalog of binary stars is not complete in the sense that the cuts we have made on the orbital parameter samplings will impart non-uniform selection biases that depend on the true orbital properties of binaries and on the cadence of observations (visits) for each source. However, because of the simple target selection and observation strategy used by APOGEE (Zasowski et al. 2013, 2017) and APOGEE-2S (south; Beaton et al., in prep., Santana et al., in prep.), we do not expect these binary-star selection biases to depend strongly on stellar parameters (e.g., metallicity, surface gravity). We can therefore still use this catalog to study the *relative* close binary fraction within our sample, but caution against interpreting the binary fractions discussed below in an absolute sense. Note that here we use "binary fraction" to mean the observed fraction of detected binary systems, not the intrinsic or birth fraction of binary systems.

Figure 5 (right) shows a near-infrared, binned color-magnitude diagram for all APOGEE sources in the subset of our sample that cross-match to the *Gaia* DR2 astrometric catalog (Gaia Collaboration et al. 2016, 2018; Lindegren et al. 2018) and have a parallax signal-to-noise $\varpi/\sigma_\varpi > 8$; we compute the absolute H-band magnitudes by converting parallax into distance as $d = 1/\varpi$. Each pixel is colored by the ratio of the number of binary star systems identified by the selections defined above (Equation 8) over the total number of sources in the parent sample; Pixels with fewer than four stars in the parent sample are white. The solid (orange) line

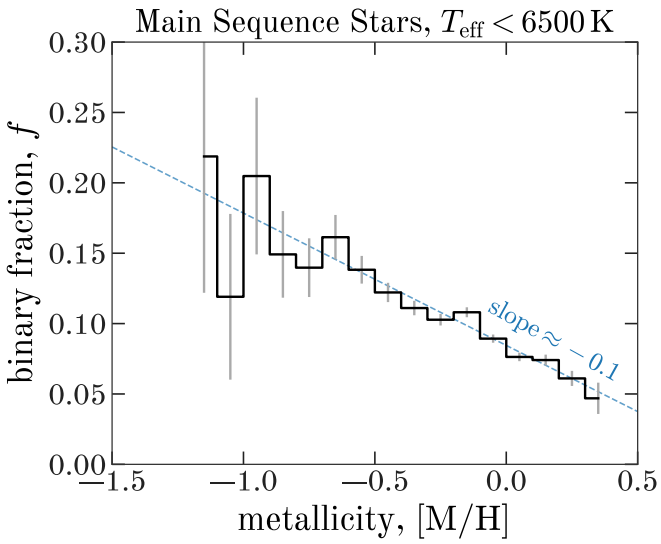

Figure 6. The observed close binary fraction as a function of bulk metallicity, [M/H]. The binary fraction is anti-correlated with metallicity, here measured with a slope of −0.1.

shows a 5 Gyr MIST isochrone Dotter (2016); Choi et al. (2016); Paxton et al. (2011, 2013, 2015) with metallicity indicated in the figure legend. The dashed line shows the equal-mass binary sequence for this isochrone, 0.75 mag above the main sequence. Note that, as expected, the binary fraction is higher in this region of the CMD, and is higher towards younger and more massive main sequence stars. Note also that the red clump (around $(J-K) \approx 0.6$, $H \approx -1.8$) has a *low* binary fraction (as noted in Badenes et al. 2018). The width of the binary sequence (in H magnitude) can be explained by the spread in metallicities in the APOGEE sample.

The top left panel of Figure 5 shows another view of the binary fraction, here shown as a 1D function of surface gravity for stars in the giant branch selection region shown in Figure 1. There is a clear and sharp dip in the occurrence of binary systems near the red clump, and the close binary fraction decreases appreciably with decreasing surface gravity (i.e., increased size). Both of these features are likely signatures of companion engulfment: As red giant stars evolve up the giant branch, any companions with orbital semi-major axes smaller than a few times the surface size of the primary star could be consumed (Ivanova et al. 2013), therefore leading to an overall decrease in the binary fraction for larger stars.

The bottom left panel shows the same, but as a function of effective temperature (as a proxy for the mass of the primary) for stars in the main sequence selection region shown in Figure 1. As has been noted in many past studies, we find that the binary fraction (companion frequency) increases with stellar mass (effective temperature) along the main sequence (e.g., Duchêne & Kraus 2013). Like the compilation of companion frequencies shown in Duchêne & Kraus (2013) and a number of studies of local samples of binary systems (e.g., Eggleton & Tokovinin 2008; Raghavan et al. 2010; Gao et al. 2014), we find that the binary fraction increases steeply for primary stellar masses $M_1 \gtrsim 1.1$ M$_\odot$ ($T_{\rm eff} \gtrsim 6000$ K).

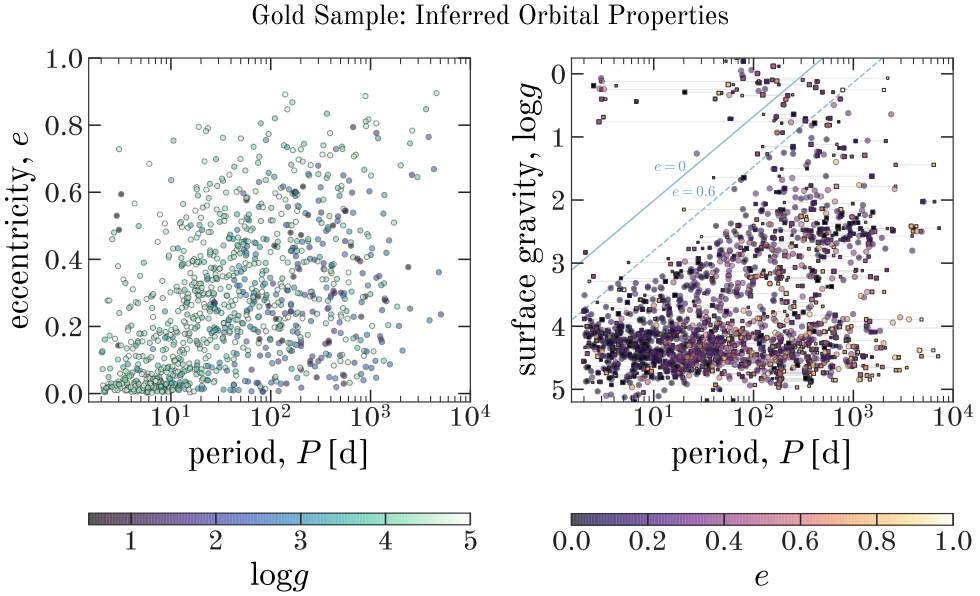

Figure 7. Left: Inferred orbital periods, P, and eccentricities, e, for *Gold Sample* systems with unimodal samplings. Markers are colored by surface gravity, $\log g$. **Right:** Similar to the left panel, but showing orbital periods and APOGEE $\log g$ measurements. The circular markers again indicate the 1 032 sources with unimodal samplings, and the square markers indicate the 492 sources with bimodal samplings, where the mean of each mode is plotted and connected by a horizontal gray line and the relative sizes of the square markers indicate the fraction of the samples that lie in each mode. The diagonal (blue) lines show the orbital period of a 0.3 $M_\odot$ companion with an orbital pericentric radius equal to the surface size of a 1.1 $M_\odot$ star with the given surface gravity and labeled eccentricity, e.

Figure 6 shows the total close binary fraction for main sequence stars as a function of bulk metallicity, [M/H]. As has been recently emphasized, we find that the fraction of close binaries is significantly anti-correlated with metallicity (Moe et al. 2019; El-Badry & Rix 2019), in disagreement with previous work (with a much smaller sample) that had found no dependency with metallicity (Jenkins et al. 2015). We find a shallower dependence of these properties, with a slope of ≈ -0.1 as compared to the previously determined slope of -0.2 (also for close binaries) (Moe et al. 2019). While we do not expect there to be strong selection biases that imprint on these quantities, we emphasize that we have not corrected for detection efficiency or completeness with our sample.

6.2. *Orbital parameter trends with stellar properties*

Figure 7 shows inferred orbital periods for all stars in the *Gold Sample* as a function of orbital eccentricity (left) and surface gravity (right), where the range of periods is clearly limited (at large P) by the The left panel clearly shows the impact of tidal circularization (e.g., Zahn 1977; Meibom & Mathieu 2005). The eccentricities of systems with $P \lesssim 10$ d are much more peaked near $e = 0$ as compared to systems with larger orbital periods (e.g., $P \gtrsim 100$ d). However, for systems with giant-star members, circularization occurs at longer periods (e.g., Price-Whelan & Goodman 2018): Systems with low eccentricities and $P > 30$ d tend to have lower $\log g$ values (darker points) as compared to systems with $P < 10$ d. In this panel, we visually

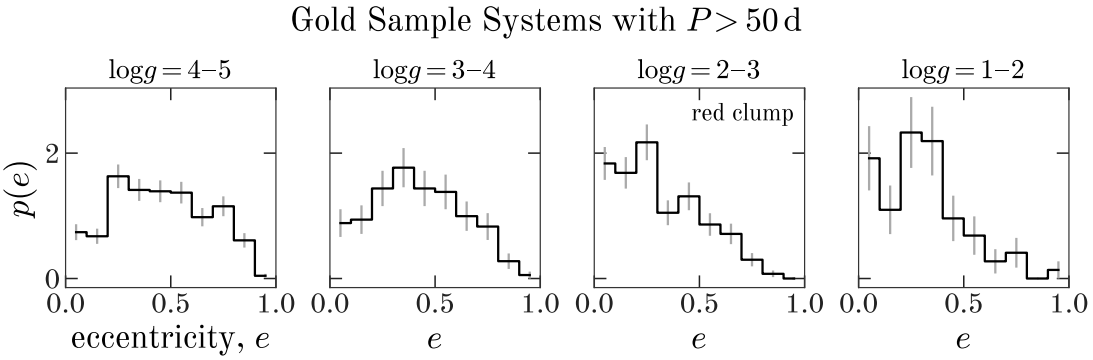

Figure 8. Histograms of maximum *a posteriori* (MAP) eccentricity values for systems with MAP $P > 50$ d. Each panel contains systems with primary star surface gravities indicated in the title.

inspected the small number of systems with $P \lesssim 5$ d and $e \gtrsim 0.4$ and found that most of these cases appear to result from systematic errors with the visit velocity data that were not removed by the quality cuts.

The right panel of Figure 7 shows orbital periods of systems in the *Gold Sample* (with unimodal or bimodal samplings) as a function of surface gravity. The diagonal lines in this panel show the orbital periods at which the orbital pericenter of a 0.3 $M_\odot$ companion is equal to the stellar surface radius for a 1.1 $M_\odot$ primary star (the median RGB mass in our sample) at the given surface gravity and eccentricity indicated. The apparent lack of systems with orbital periods shorter than or within ∼1 dex these critical lines (with $\log g \gtrsim 1$) suggests that a substantial fraction of binaries must merge or disrupt during the evolution of the primary star. The paradoxical points with seemingly small orbital periods at small $\log g$ (i.e., suggesting they orbit within the surface of the primary star) are likely due to contamination from asteroseismic modes that manifest as velocity "jitter" in low-surface-gravity giant stars. This jitter can reach amplitudes of > 1 km s^{-1} already by $\log g \approx 1$ and likely increases towards even lower values of $\log g$ (e.g., Hekker et al. 2008).

Also note the gradients in eccentricity (i.e., marker color) with respect to orbital period in the right panel of Figure 7. At a given surface gravity, there tend to be more black points (low eccentricity) closer to the stellar surface (closer to the diagonal lines). However, near the red clump ($2 \lesssim \log g \lesssim 3$), there appears to be an over-abundance of low-eccentricity points at orbital periods $P \gtrsim 100$ d. Figure 8 shows histograms of maximum *a posteriori* MAP eccentricity values for sources in the *Gold Sample* with MAP period values $P > 50$ d in four bins of surface gravity, from main sequence (farthest left) to upper giant branch (farthest right). Note that around the red clump (third panel from the left), there are significantly more $e < 0.1$ systems than expected (i.e., as compared to the previous bin). We therefore posit that systems with a primary around the red clump that have low eccentricities have likely already ascended the giant branch, whereas systems with large eccentricities are likely on their first ascent up the giant branch.

6.3. *Interesting low and high mass companions*

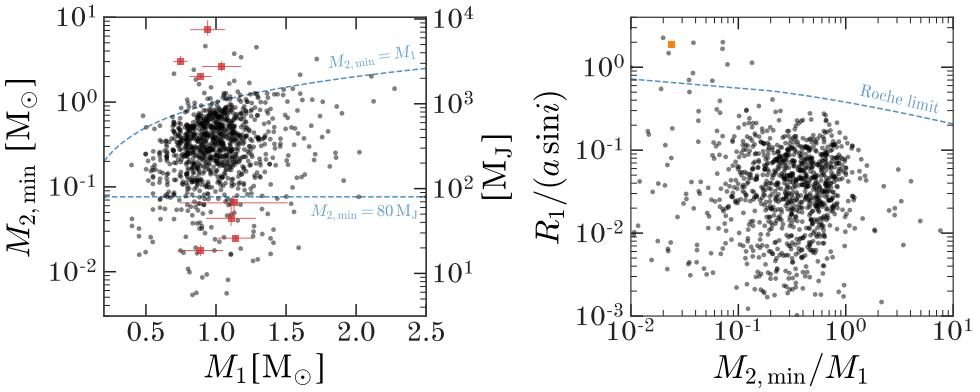

Figure 9. Left: Minimum companion masses, $M_{2,\rm min}$, as a function of primary mass, M_1, for all stars in the *Gold Sample*. The upper dashed (blue) line shows the line of equality where $M_{2,\rm min} = M_2$; Systems near or above this threshold have candidate compact object companions as the more massive secondary is fainter than the primary. The lower dashed (blue) line shows the approximate hydrogen burning limit; Sources below this threshold are candidate substellar objects. The eight highlighted points (red) are shown below in Figures 10 and 11. **Right:** The ratio of the primary stellar radius to the (projected) system orbital semi-major axis as a function of minimum mass ratio. Sources above the dashed (blue) line are likely interacting and may be photometrically variable.

By construction, all sources in the *Gold Sample* have primary stellar mass estimates, M_1, from the STARHORSE catalog (Queiroz et al. 2019). For these systems, we can then also convert the inferred orbital parameters into measurements of the minimum companion mass, $M_{2,\rm min}$ (i.e., $M_2 \sin i$ where the unknown inclination i is set to 90°). Figure 9 (left panel) shows these minimum companion mass estimates as a function of the STARHORSE primary masses for all sources in the *Gold Sample*. While the uncertainties in these quantities are not shown for most sources, the eight highlighted systems (red markers with error bars) show typical values of the errors on the masses (but note that the errors will be strongly correlated). The two dashed (blue) lines show the approximate hydrogen burning limit (lower horizontal line), and the upper curve shows the line of equality where the minimum companion mass is equal to the primary mass. Of these, 95 systems have $M_{2,\rm min} < 80$ M$_{\rm J}$: Some of these may be high-inclination stellar-mass systems, but all should be considered brown dwarf candidates. Based on the quality cuts applied to define the parent sample (which should remove sources with blended spectral lines), systems with $M_{2,\rm min} > M_1$ should not exist in the sample if the companion is luminous; The 40 systems with $M_{2,\rm min} > M_1$ are therefore excellent candidate compact object companions and will be discussed in a separate paper (Price-Whelan et al., in prep.).

The right panel of Figure 9 shows the ratio of the primary stellar radius over the (projected) system semi-major axis as a function of (minimum) mass ratio. Here, the curved, dashed line shows an estimate of the Roche radius (Eggleton 1983): Systems above this line are likely interacting. One such system (`2M08160493+2858542`), indicated by the square (orange) marker in this panel, appears to be strongly photometrically variable in data from the ASAS-SN survey (Shappee et al. 2014; Jayasinghe

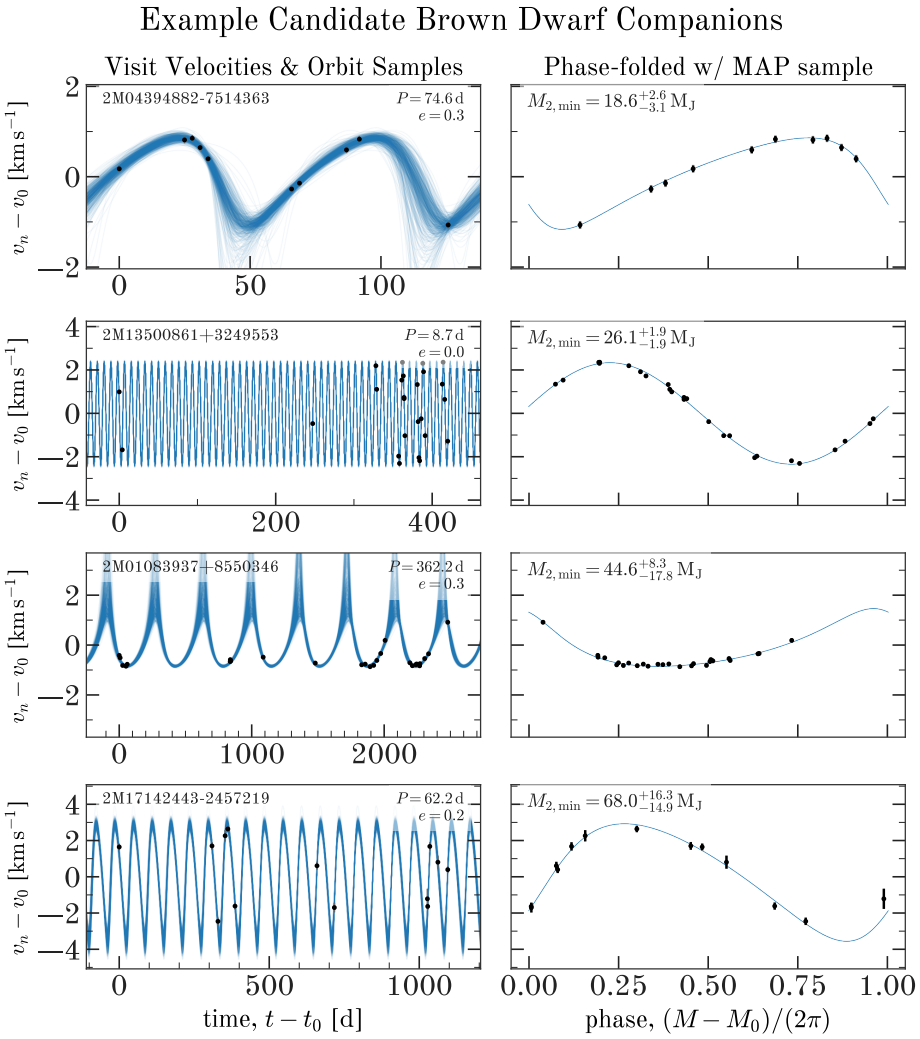

Figure 10. Example binary star systems from the *Gold Sample* with low-mass companions that are candidate substellar objects. Each row is a different source (indicated in the left panels). The left panels show the raw visit velocity data (black markers) under-plotted with orbits computed from the posterior samples for each source (blue lines). The right panels show the same data phase-folded with the MAP orbit sample period and under-plotted with an orbit computed from the MAP sample. The minimum companion mass for each system is indicated in the right panels.

et al. 2019), however most other candidate interacting systems do not have ASAS-SN light curves and could instead be followed up with TESS (Ricker et al. 2014).

Figure 10 shows the radial velocity data (black markers)—under-plotted (blue lines) with orbits computed from posterior samples—for the four highlighted systems below the 80 M_J line in Figure 9 (left). The left panels show the time series, and the right panels show the same data and orbits, but now phase-folded using the MAP period value. The inferred minimum companion masses are indicated on each right panel. These systems were chosen from a vetted subsample of all substellar companion candidates to highlight systems with a range of companion masses, eccentricities, and numbers of observations.

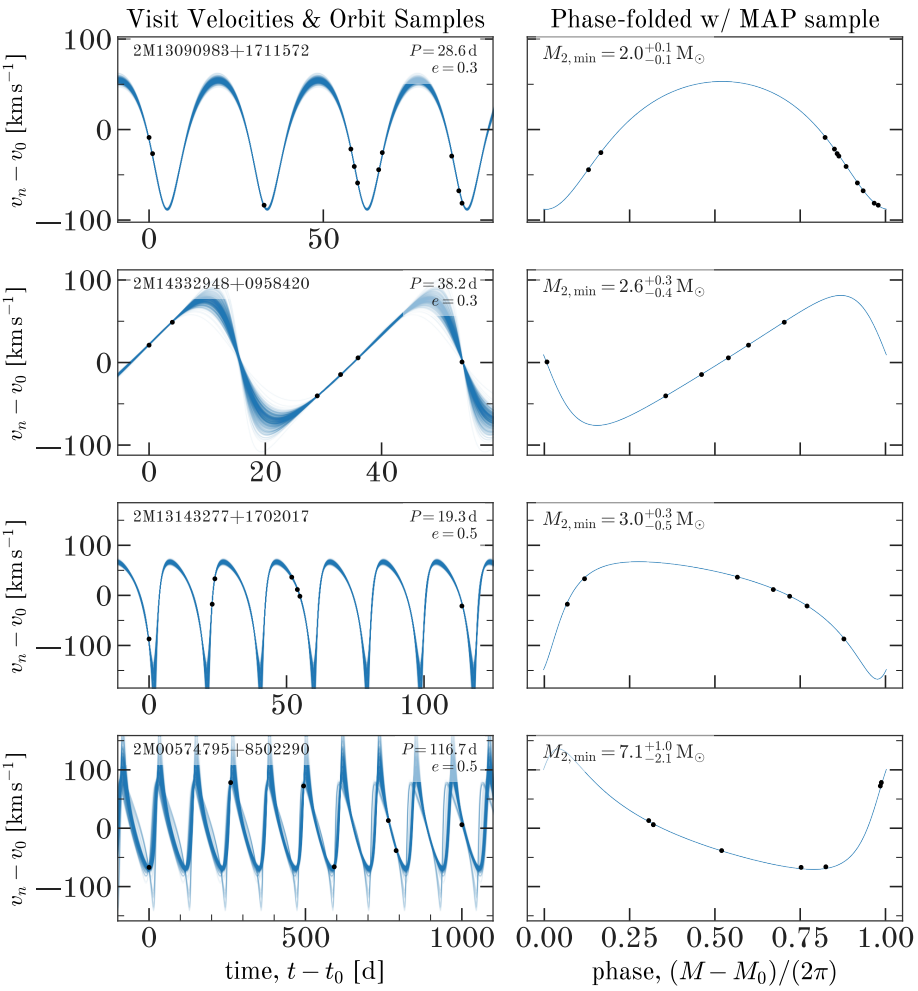

Figure 11. The same as Figure 10, but for example binary star systems from the *Gold Sample* with faint, high-mass companions that are candidate compact objects.

Figure 11 shows the same, but for the four highlighted systems above the $M_{2,\mathrm{min}} = M_1$ line in Figure 9. The companions in the systems shown in the top two rows are just barely consistent with being high-mass neutron stars (e.g., Cromartie et al. 2019), but the systems shown in the bottom two rows contain candidate non-interacting black hole companions (these are discussed in more detail in the companion paper; Price-Whelan et al., in prep.). The recently discovered non-interacting black hole–giant star system (that made use of APOGEE data; Thompson et al. 2019) does not appear in our candidates because it only has 3 visit spectra with APOGEE data alone and thus does not pass the strict cuts we used to construct the *Gold Sample*.

6.4. *Hierarchical inference of the eccentricity distribution*

Most of the results highlighted above make use of the catalogs created from defining selections on the posterior samplings generated with *The Joker*. However, the real power in the individual system posterior samplings is that they enable further *hierarchical* modeling of binary-star population properties without having to make

hard cuts on the samples. In future work, we will use these samplings to construct a joint model for the period, eccentricity, and mass ratio distributions of binary stars as a function of stellar parameters, but this will also require modeling the sample selection function and our detection efficiency. While the full hierarchical inference is out of scope for this *Article*, here we demonstrate how this could be done using a simpler, toy problem: Inferring the eccentricity distribution of long-period binary stars using a parametric model.

We first select all 53 790 sources with samplings from *The Joker* (or subsequent MCMC) with 4000 K $< T_{\rm eff} <$ 7000 K and $-2 <$ [M/H] < 0.5 in order to select main sequence, FGK-type stars. We then only keep 8 599 sources that have > 128 samples with $P > 100$ d and $K > 1$ km s^{-1}, of which 158 sources have unimodal samplings (i.e., generated with MCMC). The second criteria (on velocity semi-ampitude, K) would not be necessary if we instead constructed a mixture model with components to represent stars with companions and the background population, but here, for simplicity, we instead just make a cut on the posterior samplings. For each j source in this sample of binaries with FGK-type primary stars, we then have M_j (up to 512) samples in orbital eccentricity, e_{jm}. We parametrize the eccentricity distribution using a beta distribution, $B(a, b)$, and use the importance sampling trick to reweight the e_{jm} samples to infer the hyperparameters (a, b) (Hogg et al. 2010).

In detail, we would like to evaluate or generate samples from the posterior probability distribution over the hyperparameters of the eccentricity distribution

$$p(a, b \,|\, D) \propto p(D \,|\, a, b)\, p(a, b) \tag{9}$$

where D represents all visit data for all sources, i.e.,

$$p(D \,|\, a, b) = \prod_j p(D_j \,|\, a, b) \tag{10}$$

and (a, b) are the parameters of our assumed beta distribution model. There is no obvious way to evaluate this posterior probability—especially the likelihood term—given the hyperparameters. However, recall that we have samplings from the per-source posterior distributions over eccentricity,

$$p(e_j \,|\, D_j, \alpha_0) \propto p(D_j \,|\, e_j)\, p(e_j \,|\, \alpha_0) \tag{11}$$

$$e_{jm} \sim p(e \,|\, D_j, \alpha_0) \tag{12}$$

where α_0 is meant to represent the parameters of our assumed "interim" prior over eccentricity that we used to generate the per-source samplings (i.e., see Table 1), and here "$\sim$" means "is sampled from." Through math that is explained in more detail in other work (e.g., Hogg et al. 2010; Price-Whelan et al. 2018), it turns out that the hierarchical likelihood can be written as a sum over the ratio of probabilities

$$p(D_j \,|\, a, b) \approx \frac{\mathcal{Z}}{M_j} \sum_k^M \frac{p(e_{jm} \,|\, a, b)}{p(e_{jm} \,|\, \alpha_0)} \tag{13}$$

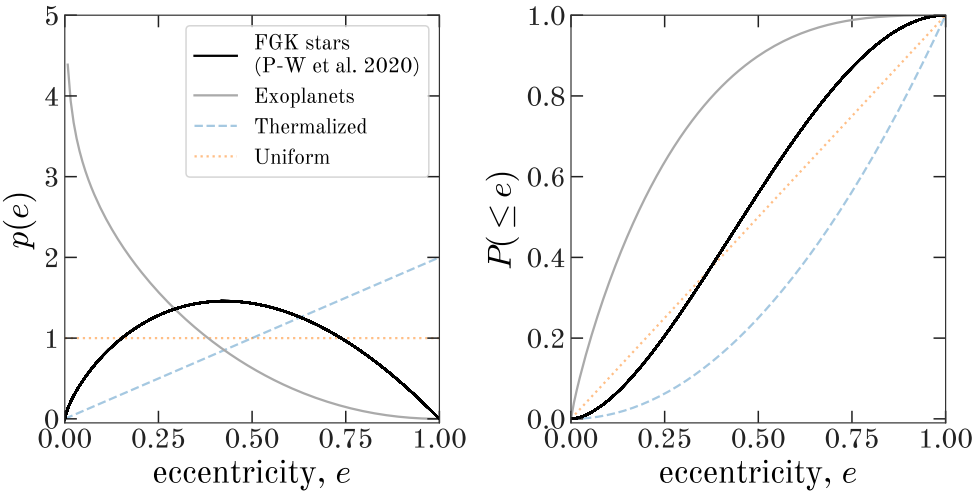

Figure 12. Left: The inferred eccentricity distribution for binary star systems with FGK-type primary stars (black line). We use the posterior sampings for 8 599 sources within a toy hierarchical model of the eccentricity distribution, represented as a beta distribution. We also plot common eccentricity distributions from the literature, such as the global exoplanet model from (Kipping 2013, ; solid, gray line), the (theoretical) thermalized population (Jeans 1919, ; dashed, blue line), and a uniform distribution (dotted, orange line). **Right:** The same as the left panel, but showing cumulative distribution functions instead.

where $\mathcal{Z}$ is a normalization constant. In practice, we evaluate the hierarchical log-likelihood, $\ln p(D_j \,|\, a, b)$, as

$$\ln p(D \,|\, a, b) = \sum_j \left[\underset{m}{\text{logsumexp}} \left(\ln p(e_{jm} \,|\, a, b) - \ln p(e_{jm} \,|\, \alpha_0) \right) - \ln M_j \right] \quad . \tag{14}$$

With a method for evaluating the hierarchical likelihood (Equation 9), we now just need to specify prior probability distributions over the hyperparameters of the beta distribution (a, b). For each parameter, we use a uniform distribution over the domain $(0.1, 10)$. We implement this model, including the sums over the eccentricity samples, within the context of a `pymc3` model and use the built-in NUTS sampler to generate posterior samples in the parameters of the eccentricity distribution. We run the sampler for 1000 steps to tune, then run four chains in parallel, each for an additional 2000 steps. We assess convergence again by computing the Gelman-Rubin statistic, $\hat{R}$ and find that all parameters have converged samplings at the end of our run.

From these posterior samples, we find $a = 1.749 \pm 0.001$ and $b = 2.008 \pm 0.001$. Figure 12 shows the inferred eccentricity distribution (black curve, left panel) and the corresponding cumulative distribution function (right panel) along with some other eccentricity distributions from the literature. For example, the (global) exoplanet eccentricity distribution from Kipping (2013), the (theoretical) eccentricity distribution for a thermalized population of binaries (Jeans 1919), and a uniform distribution. At long periods, binary star systems seem to have moderate eccentricities that disfavor circular or very eccentric values. This is in agreement with past studies that have

focused on nearby samples of solar-type stars with smaller sample sizes (e.g., Duquennoy & Mayor 1991; Raghavan et al. 2010). Note, however, that this should still be viewed as a demonstration: Future analysis should assess the impact of selection effects and detection efficiency on the inferred eccentricity distribution using these data. We also emphasize that the extremely precise constraints we get on the parameters of the beta distribution imply that we have enough data to complexify the model, either by using non-parametric forms for the eccentricity distribution to move away from rigid models or by parametrizing variations in the distribution with stellar parameters.

7. DISCUSSION

In what follows, we discuss some important caveats and considerations for interpreting the results and using the catalogs described in this *Article*.

7.1. *Assumptions, caveats, and known failures*

The assumptions that underlie the sampling procedure described above are enumerated in Section 3.1 in Price-Whelan et al. (2018). We therefore briefly rephrase the most important implications of these assumptions as a set of caveats and points of caution for any users of the posterior samplings released with this *Article*.

First, despite allowing for a per-source, additive (in variance) extra uncertainty parameter (s in Table 1), we are very sensitive to outliers, or, more generally, any visit velocities with strongly non-Gaussian noise properties. In APOGEE, this might occur for blended sources, multiple-star systems with more than one star that contribute significantly to infrared flux, or sources with stellar parameters very beyond the grid of template spectra (Nidever et al. 2015).

Second, related to the first point, we make the strong assumption that all sources are single-lined, i.e., that any binary companions do not contribute significantly to the observed spectra. This is wrong in general: Some systems will be double lined (sometimes only subtly, but detectable, e.g., El-Badry et al. 2018), and we will be biased in cases where these sources are not properly filtered by the quality cuts done above. This also means that we will definitely miss systems with similar masses (and especially "twin" binaries; El-Badry et al. 2019). We expect this assumption to be worse on the main sequence than on the giant branch, because any lower-mass companion to a giant branch star will have a luminosity hundreds or thousand times fainter.

Third, the adopted prior *pdf* over systemic velocities, v_0, is reasonable for considering all APOGEE sources (i.e., for a mixture of kinematically disk-like and halo-like sources), but may lead to biased posterior samplings for sources in globular clusters or dwarf galaxies. For such systems, it would be safer to re-run *The Joker* with specialized priors over systemic velocity for each individual host system.

Fourth, in this work, we assume that all systems are binary systems, so triples or higher-order stellar multiplets will generally have incorrect samplings. We will generate samplings for systems that are consistent with being hierarchical triple-star systems, but this is beyond the scope of the general-use catalog considered here.

Finally, related to the fourth point, we assume that all velocity variations represent orbital motion (i.e., not pulsation or similar intrinsic stellar phenomena). As highlighted in Figure 5, this assumption is clearly violated when $\log g \lesssim 1$ km s^{-1} where stellar surface jitter masquerades as orbital motion and leads to (a small amount of) contamination.

7.2. *Binary fraction trends with stellar properties*

We find a number of interesting trends in the binary fraction as a function of stellar parameters and chemical composition that have far-reaching implications. For one, the binary fraction increases rapidly with decreasing metallicity (as also noted recently by Moe et al. 2019; El-Badry & Rix 2019). Beyond the implications discussed in Moe et al. (2019), this also motivates appropriate investigation into how a large binary fraction could influence inferred properties of dwarf galaxies and globular clusters. For example, stellar binarity impacts velocity dispersion measurements, which then contaminate estimates of dark matter masses in these systems (e.g., Aaronson & Olszewski 1987; Kouwenhoven & de Grijs 2008; Spencer et al. 2017, 2018), but also impact the long-term stability and dynamical evolution of compact stellar systems (e.g., Hut et al. 1992; Sigurdsson & Phinney 1993). A large binary fraction also impacts the chemical evolution of these systems (e.g., Eldridge et al. 2008; Eldridge & Stanway 2009).

We caution, however, that any real understanding of the binary fraction (in an absolute sense) from the *catalogs* produced here will require a model of the APOGEE selection function and for our detection efficiency. Still, we clearly now have samples of binary stars large enough to begin placing strong constraints on theories of binary star formation and evolution and their impact on galactic stellar populations.

7.3. *Selection, completeness, false positives, and contamination*

As cautioned above, to properly use our catalog of systems for performing statistical tests (for example, to interpret the binary fraction values in Figure 5 in an absolute sense), it is critical to have estimates of our detection efficiency or completeness as a function of binary orbital parameters and stellar parameters. While we have not provided estimates of the completeness, we do release the full posterior samplings in orbital parameters for *all* sources, along with open-source software that could be used to construct these estimates. In general, our completeness will likely be a strong function of velocity semi-amplitude, period, and eccentricity (which implicitly imply functions of companion mass, inclination, and separation). It will also depend on mass ratio, as many sources with bright companions will be dropped by the quality cuts imposed on the APOGEE data. As a consequence of this, the systems considered in this work are primarily close binary systems with intermediate mass ratios.

One way to construct completeness estimates would be to repeat the analysis done in this *Article* using simulated systems with known parameters. The sampler used to generate the posterior orbit samplings is open source and released as a `Python` package (Price-Whelan et al. 2017; Price-Whelan & Hogg 2019). The pipeline software

used to define and analyze the APOGEE parent sample is open source and is also available as a `Python` package, `hq` (Price-Whelan 2019).

7.4. *Below-threshold searches*

Another problem with a traditional catalog of detected binary companions (like ours) is that there are many sources in which the hypothesis of a single star is clearly rejected, but not strong enough to qualify as a reliable binary "detection." A user who has informative data for a source that would take a sub-threshold source above threshold (in terms of our criteria for including a source in the catalog) has no recourse if only given the rigidly-thresholded catalog entries. Even for well detected binary systems, in a traditional catalog of orbital parameters, there is no simple way to combine the results with new data to improve or adjust parameter estimates. The samplings provided here can be used to solve these problems; They can be used to combine the APOGEE information with new data, without requiring an *ab initio* re-analysis of the original APOGEE data. This can be done by repeating the rejection sampling step used in *The Joker* to generate posterior samples, but replacing the prior samples with the posterior samples generated with the APOGEE data alone and replacing the full marginal likelihood evaluation with the marginal likelihood of the new data computed at each sample.

In detail, following the notation in Appendix A, converting the posterior samples released here into posterior samples over the APOGEE data, D_1, *plus* some new velocity data, D_2, requires generating samples from the posterior *pdf*

$$p(\boldsymbol{\theta} \,|\, D_1, D_2) \propto p(D_1 \,|\, \boldsymbol{\theta})\, p(D_2 \,|\, \boldsymbol{\theta})\, p(\boldsymbol{\theta}) \tag{15}$$

$$\propto p(D_2 \,|\, \boldsymbol{\theta})\ [p(D_1 \,|\, \boldsymbol{\theta})\, p(\boldsymbol{\theta})] \tag{16}$$

where we have assumed that the new data are independent of the APOGEE data. Note that the terms in brackets in Equation 16 are proportional to the posterior probability of the parameters given only the APOGEE data, i.e., the distribution we have generated samples from using *The Joker*. We can therefore use the posterior samples generated from the *The Joker* with the APOGEE data to rejection-sample using the new marginal likelihood, $p(D_2 \,|\, \boldsymbol{\theta})$, to generate samples from $p(\boldsymbol{\theta} \,|\, D_1, D_2)$.

The ability to perform sub-threshold searches or add external information is limited by detailed shape of the posterior *pdf* and the number of samples we deliver (here, 512). If the new data are highly informative, or favor a mode in the posterior *pdf* that is not well sampled, the posterior samplings we deliver will not be dense enough to provide support for the updated posterior *pdf*. This puts limitations on the scope of sub-threshold searches, but at least they are possible with these outputs, in some regime of applicability.

8. CONCLUSIONS

Our key results and conclusions are summarized below:

The close binary fraction depends on the stellar parameters of the primary star: Figure 5 shows a simple estimate of the close binary fraction over the

color–magnitude diagram, utilizing all 232 531 APOGEE sources used in this work. There is a notable dearth of close companions around the red clump, where companions may have been engulfed when the primary star ascended the upper giant branch. We also rediscover trends in the binary fraction with effective temperature along the main sequence (i.e., stellar mass), and show that the binary fraction on the giant branch depends on the surface gravity (i.e., surface size) of the primary, also indicating that companion engulfment is an important outcome of close binary star evolution.

The binary fraction is anti-correlated with metallicity: We find that the binary fraction decreases linearly with bulk metallicity with a slope of -0.1 dex^{-1} over the domain $-1 \lesssim$ [M/H] $\lesssim 0.4$, as shown in Figure 6.

We detect the clear signature of tidal circularization in field main sequence and red giant branch stars: Figure 7 (left) shows inferred periods and eccentricities for systems with uniquely-determined orbits in the *Gold Sample*. The abundances of low-eccentricity sources at short periods is a manifestation of tidal circularization, which should operate at longer periods for larger, more convective (i.e., giant branch) stars.

We identify 95 candidate brown dwarf companions: Using simplistic cuts on the *Gold Sample* of high-quality sources with unimodal posterior samplings, we identify candidate brown dwarf companions by selecting sources with median minimum companion mass ($M_{2,\mathrm{min}}$) values below the hydrogen burning limit, $M_{2,\mathrm{min}} < 80\ \mathrm{M_J}$. Figure 9 (left) shows these sources as points below the horizontal dashed line. We highlight a few of these systems in Figure 10.

We identify 40 candidate non-interacting compact object companions: Again using simplistic cuts on the *Gold Sample* of high-quality sources with unimodal posterior samplings, we identify candidate compact object companions by selecting sources with $M_{2,\mathrm{min}} > M_1$. Figure 9 (left) shows these sources as points above the upper, curved dashed line. We highlight a few of these systems in Figure 11.

The binary-star eccentricity distribution is peaked at moderate eccentricities: We execute a toy hierarchical inference using the posterior samplings for $\sim 8\,600$ FGK-type main sequence stars to infer the eccentricity distribution of long-period ($P > 100$ d), intermediate-mass main-sequence star binary systems. By representing the distribution using a beta distribution, we derive precise posterior constraints on the parameters using this hierarchical model and find $a = 1.749 \pm 0.001$ and $b = 2.008 \pm 0.001$. Figure 12 shows our inferred eccentricity distribution, indicating that long-period binary star systems prefer moderate eccentricities.

We release a sample of 20 000 binary star systems and posterior samplings over orbital parameters for 232 531 APOGEE sources: Finally, we release

a catalog of 19 635 high-confidence binary star systems (Table 2). The majority of these systems have poorly constrained orbital parameters, but we release posterior samplings over these parameters for all 232 531 APOGEE sources to enable other probabilistic inferences with these data. We also define and release a *Gold Sample* containing 1 032 systems with high-quality, unimodal posterior samplings that can be used and summarized more simply.

ACKNOWLEDGMENTS

It is a pleasure to thank Borja Anguiano (Virginia), Carles Badenes (Pittsburgh), Evan Bauer (KITP), Lars Bildsten (KITP), Dan Foreman-Mackey (Flatiron), Will Farr (Flatiron), Marla Geha (Yale), and Adam Jermyn (Flatiron) for useful discussions. APW acknowledgements support and space from the Max-Planck-Institut für Astronomie during initial work on this project. PMF acknowledge support for this research from the National Science Foundation (AST-1311835 & AST-1715662). JGF-T is supported by FONDECYT No. 3180210 and Becas Iberoamérica Investigador 2019, Banco Santander Chile. DAGH acknowledges support from the State Research Agency (AEI) of the Spanish Ministry of Science, Innovation and Universities (MCIU) and the European Regional Development Fund (FEDER) under grant AYA2017-88254-P. SH is supported by an NSF Astronomy and Astrophysics Postdoctoral Fellowship under award AST-1801940.

Funding for the Sloan Digital Sky Survey IV has been provided by the Alfred P. Sloan Foundation, the U.S. Department of Energy Office of Science, and the Participating Institutions. SDSS-IV acknowledges support and resources from the Center for High-Performance Computing at the University of Utah. The SDSS web site is www.sdss.org.

SDSS-IV is managed by the Astrophysical Research Consortium for the Participating Institutions of the SDSS Collaboration including the Brazilian Participation Group, the Carnegie Institution for Science, Carnegie Mellon University, the Chilean Participation Group, the French Participation Group, Harvard-Smithsonian Center for Astrophysics, Instituto de Astrofísica de Canarias, The Johns Hopkins University, Kavli Institute for the Physics and Mathematics of the Universe (IPMU) / University of Tokyo, Lawrence Berkeley National Laboratory, Leibniz Institut für Astrophysik Potsdam (AIP), Max-Planck-Institut für Astronomie (MPIA Heidelberg), Max-Planck-Institut für Astrophysik (MPA Garching), Max-Planck-Institut für Extraterrestrische Physik (MPE), National Astronomical Observatories of China, New Mexico State University, New York University, University of Notre Dame, Observatário Nacional / MCTI, The Ohio State University, Pennsylvania State University, Shanghai Astronomical Observatory, United Kingdom Participation Group, Universidad Nacional Autónoma de México, University of Arizona, University of Colorado Boulder, University of Oxford, University of Portsmouth, University of Utah, University of Virginia, University of Washington, University of Wisconsin, Vanderbilt University, and Yale University.

Software: Astropy (Astropy Collaboration et al. 2013, 2018), apred (Nidever et al. 2015), ASPCAP (García Pérez et al. 2016), exoplanet (Foreman-Mackey et al. 2019), gala (Price-Whelan 2017), IPython (Pérez & Granger 2007), numpy (Walt et al. 2011), pymc3 (Salvatier et al. 2016), schwimmbad (Price-Whelan & Foreman-Mackey 2017), scipy (Jones et al. 2001–), theano (Al-Rfou et al. 2016), thejoker (Price-Whelan et al. 2017; Price-Whelan & Hogg 2019)

APPENDIX

A. UPDATE TO THE MARGINAL LIKELIHOOD EXPRESSION FOR *The Joker*

As noted above (see Section 3.1), the assumptions in Price-Whelan et al. (2017) that lead to the simplified form of the marginal likelihood (Equation 11 in Price-Whelan et al. 2017) are not valid. We therefore here re-derive the marginal likelihood that forms the basis of the implementation of *The Joker* used in this work.

For each APOGEE source, we have a set of N radial velocity measurements (visits) v_n at times t_n with uncertainties σ_n. Under the assumption that the source is in a binary star system, our model for the true radial velocity of the source at any time is given by Equation 2 above. Our goal (as in Price-Whelan et al. 2017) is to analytically marginalize over the linear parameters in Equation 2—(K, v_0)—under the assumption that the uncertainties on each radial velocity measurement are Gaussian and independent. To do this, we must write down expressions for the likelihood, and for the prior probability distribution over the parameters that we will be marginalizing over (i.e., the linear parameters). We have already made the assumption that our likelihood has a Gaussian form, so to do this marginalization conveniently and analytically, we additionally assume that the prior *pdf* also has a Gaussian form. Under these assumptions, the solution to this marginalization is given in Hogg et al. (in prep.).

To see the relation between the specific problem solved by *The Joker* and the derivation in Hogg et al. (in prep.), it will be convenient to repackage our data and linear parameters as

$$\boldsymbol{y} = (v_1, v_2, \ldots, v_N)^\mathsf{T} \tag{A1}$$

$$\boldsymbol{x} = (K, v_0)^\mathsf{T} \tag{A2}$$

$$\mathbf{C} = \begin{pmatrix} \sigma_1^2 & 0 & \cdots & 0 \\ 0 & \sigma_2^2 & \cdots & 0 \\ & & \ddots & \\ 0 & 0 & \cdots & \sigma_N^2 \end{pmatrix} \tag{A3}$$

and to assume that the mean and covariance matrix of the prior over the linear parameters are given by $\boldsymbol{\mu}, \boldsymbol{\Lambda}$, respectively. Given a set of nonlinear parameters

$\boldsymbol{\theta} = (P, e, \omega, M_0)$, we will also need to define a design matrix, $\mathbf{M}$,

$$\mathbf{M} = \begin{pmatrix} \zeta(t_1\,;\,\boldsymbol{\theta}) & 1 \\ \zeta(t_2\,;\,\boldsymbol{\theta}) & 1 \\ \vdots & \vdots \\ \zeta(t_N\,;\,\boldsymbol{\theta}) & 1 \end{pmatrix} \tag{A4}$$

where $\zeta(\cdot)$ is given by Equation 3. With these assumptions, the marginalized likelihood, Q, for a source, given nonlinear parameters $\boldsymbol{\theta}$, can be written

$$Q = \int \mathrm{d}\boldsymbol{x}\, \mathcal{N}(\boldsymbol{y}\,|\,\mathbf{M}\cdot\boldsymbol{x}, \mathbf{C})\, \mathcal{N}(\boldsymbol{x}\,|\,\boldsymbol{\mu}, \boldsymbol{\Lambda}) \tag{A5}$$

$$= \int \mathrm{d}\boldsymbol{x}\, \mathcal{N}(\boldsymbol{x}\,|\,\boldsymbol{a}, \mathbf{A})\, \mathcal{N}(\boldsymbol{y}\,|\,\boldsymbol{b}, \mathbf{B}) \tag{A6}$$

$$= \mathcal{N}(\boldsymbol{y}\,|\,\boldsymbol{b}, \mathbf{B}) \tag{A7}$$

$$\boldsymbol{b} = \mathbf{M}\cdot\boldsymbol{\mu} \tag{A8}$$

$$\mathbf{B} = \mathbf{C} + \mathbf{M}\cdot\boldsymbol{\Lambda}\cdot\mathbf{M}^{\mathsf{T}} \tag{A9}$$

where the integral becomes simple because the second normal distribution, $\mathcal{N}(\boldsymbol{y}\,|\,\boldsymbol{b}, \mathbf{B})$, does not depend on the integration variables, $\boldsymbol{x}$, and the integral over the first normal distribution is 1 Hogg et al. (in prep.). A final point that is relevant to additional enhancements discussed in Section 3.1 (and is exploited in this *Article*) is to note that $\boldsymbol{\mu}$ and $\boldsymbol{\Lambda}$ *can* depend on the nonlinear parameters.

B. DATA TABLES

The primary data product released with this *Article* are the posterior samplings generated for each of 232 531 sources in APOGEE DR16. However, we also compute summary information and statistics about these samplings and provide these data in Table 2. We also define a *Gold Sample* of high-quality, uniquely-solved binary star systems (see Section 6.2) and release summary information along with cross-matched data from *Gaia* DR2 and the STARHORSE catalog of stellar parameters in Table 3.

REFERENCES

Aaronson, M., & Olszewski, E. 1987, in IAU Symposium, Vol. 117, Dark matter in the universe, ed. J. Kormendy & G. R. Knapp, 153

Abbott, B. P., Abbott, R., Abbott, T. D., et al. 2016, Phys. Rev. Lett., 116, 061102, doi: 10.1103/PhysRevLett.116.061102

—. 2019, Phys. Rev. X, 9, 031040, doi: 10.1103/PhysRevX.9.031040

Abolfathi, B., Aguado, D. S., Aguilar, G., et al. 2017, ArXiv e-prints. https://arxiv.org/abs/1707.09322

Ahumada, R., Allende Prieto, C., Almeida, A., et al. 2019, arXiv e-prints, arXiv:1912.02905. https://arxiv.org/abs/1912.02905

Al-Rfou, R., Alain, G., Almahairi, A., et al. 2016, arXiv e-prints, abs/1605.02688. http://arxiv.org/abs/1605.02688

Astropy Collaboration, Robitaille, T. P., Tollerud, E. J., et al. 2013, A&A, 558, A33, doi: 10.1051/0004-6361/201322068

Metadata for all sources in the parent sample

Column name	Unit / format	Description
APOGEE_ID		APOGEE source identifier
n_visits		number of visits that pass our quality cuts
MAP_P	d	P, orbital period
MAP_P_err	d	
MAP_e		e, orbital eccentricity
MAP_e_err		
MAP_omega	rad	ω, argument of pericenter
MAP_omega_err	rad	
MAP_M0	rad	M_0, phase at reference epoch
MAP_M0_err	rad	
MAP_K	$\mathrm{km\,s^{-1}}$	K, velocity semi-amplitude
MAP_K_err	$\mathrm{km\,s^{-1}}$	
MAP_v0	$\mathrm{km\,s^{-1}}$	v_0, systemic velocity
MAP_v0_err	$\mathrm{km\,s^{-1}}$	
MAP_s	$\mathrm{km\,s^{-1}}$	s, excess variance parameter
MAP_s_err	$\mathrm{km\,s^{-1}}$	
t0_bmjd		reference epoch (Barycentric MJD)
baseline	d	the time baseline of the visits
MAP_ln_likelihood		the log-marginal-likelihood value of the MAP sample
MAP_ln_prior		the log-prior value of the MAP sample
max_unmarginalized_ln_likelihood		the maximum value of the unmarginalized likelihood
max_phase_gap		the maximum gap in phase of the data for the MAP sample
periods_spanned		the number of (MAP) periods spanned by the data
phase_coverage		the phase-coverage of the data folded on the MAP period
phase_coverage_per_period		the maximum number of data points within a single MAP period
unimodal	boolean	True if the sampling is unimodal in period
joker_completed	boolean	True if the source has 512 samples from *The Joker*
mcmc_completed	boolean	True if the source has 512 samples from MCMC
mcmc_success	boolean	True if the MCMC sampling converged
gelman_rubin_max		The maximum (over parameters) value of $\hat{R}$
robust_constant_ln_likelihood		The maximum log-likelihood value of a robust constant-velocity fit to the visit data
binary_catalog	boolean	True if the source is in the binary catalog (Section 5)

(232 531 rows)

Table 2. Description of the metadata table containing summary information for all APOGEE sources in the parent sample. All columns ending in `_err` are estimates of the standard-deviation of the posterior samples around the MAP sample, but only computed for unimodal samplings.

Metadata for the *Gold Sample*

Column name	Unit / format	Description
`APOGEE_ID`		APOGEE source identifier
`mass`	$M_\odot$	mass of the primary, from the STARHORSE catalog
`mass_err`	$M_\odot$	uncertainty on the primary mass
`m2_min_1`	$M_\odot$	1st percentile value of $M_{2,\mathrm{min}}$
`m2_min_5`	$M_\odot$	5th percentile value of $M_{2,\mathrm{min}}$
`m2_min_16`	$M_\odot$	16th percentile value of $M_{2,\mathrm{min}}$
`m2_min_50`	$M_\odot$	median value of $M_{2,\mathrm{min}}$
`m2_min_84`	$M_\odot$	84th percentile value of $M_{2,\mathrm{min}}$
`m2_min_95`	$M_\odot$	95th percentile value of $M_{2,\mathrm{min}}$
`m2_min_99`	$M_\odot$	99th percentile value of $M_{2,\mathrm{min}}$
⋮		all columns from Table 2
⋮		all columns from APOGEE `allStar` file
⋮		all columns from *Gaia* DR2 `gaia_source` table

(1 032 rows)

Table 3. Description of the data table containing summary information for all sources in the *Gold Sample*.

Astropy Collaboration, Price-Whelan, A. M., Sipócz, B. M., et al. 2018, AJ, 156, 123, doi: 10.3847/1538-3881/aabc4f

Badenes, C., Mazzola, C., Thompson, T. A., et al. 2018, ApJ, 854, 147, doi: 10.3847/1538-4357/aaa765

Blanton, M. R., Bershady, M. A., Abolfathi, B., et al. 2017, AJ, 154, 28, doi: 10.3847/1538-3881/aa7567

Bowen, I. S., & Vaughan, A. H., J. 1973, ApOpt, 12, 1430, doi: 10.1364/AO.12.001430

Choi, J., Dotter, A., Conroy, C., et al. 2016, ApJ, 823, 102, doi: 10.3847/0004-637X/823/2/102

Cottaar, M., Covey, K. R., Meyer, M. R., et al. 2014, ApJ, 794, 125, doi: 10.1088/0004-637X/794/2/125

Cromartie, H. T., Fonseca, E., Ransom, S. M., et al. 2019, Nature Astronomy, 439, doi: 10.1038/s41550-019-0880-2

Dotter, A. 2016, ApJS, 222, 8, doi: 10.3847/0067-0049/222/1/8

Duchêne, G., & Kraus, A. 2013, ARA&A, 51, 269, doi: 10.1146/annurev-astro-081710-102602

Duquennoy, A., & Mayor, M. 1991, A&A, 500, 337

Eggleton, P. P. 1983, ApJ, 268, 368, doi: 10.1086/160960

Eggleton, P. P., & Tokovinin, A. A. 2008, MNRAS, 389, 869, doi: 10.1111/j.1365-2966.2008.13596.x

El-Badry, K., & Rix, H.-W. 2019, MNRAS, 482, L139, doi: 10.1093/mnrasl/sly206

El-Badry, K., Rix, H.-W., Tian, H., Duchêne, G., & Moe, M. 2019, MNRAS, 489, 5822, doi: 10.1093/mnras/stz2480

El-Badry, K., Rix, H.-W., Ting, Y.-S., et al. 2018, MNRAS, 473, 5043, doi: 10.1093/mnras/stx2758

Eldridge, J. J., Izzard, R. G., & Tout, C. A. 2008, MNRAS, 384, 1109, doi: 10.1111/j.1365-2966.2007.12738.x

Eldridge, J. J., & Stanway, E. R. 2009, MNRAS, 400, 1019, doi: 10.1111/j.1365-2966.2009.15514.x

Eldridge, J. J., Stanway, E. R., Xiao, L., et al. 2017, PASA, 34, e058, doi: 10.1017/pasa.2017.51
Fernández-Trincado, J. G., Mennickent, R., Cabezas, M., et al. 2019, A&A, 631, A97, doi: 10.1051/0004-6361/201935369
Foreman-Mackey, D., Czekala, I., Luger, R., et al. 2019, dfm/exoplanet, doi: 10.5281/zenodo.1998447
Gaia Collaboration, Prusti, T., de Bruijne, J. H. J., et al. 2016, A&A, 595, A1, doi: 10.1051/0004-6361/201629272
Gaia Collaboration, Brown, A. G. A., Vallenari, A., et al. 2018, A&A, 616, A1, doi: 10.1051/0004-6361/201833051
Gao, S., Liu, C., Zhang, X., et al. 2014, ApJL, 788, L37, doi: 10.1088/2041-8205/788/2/L37
García Pérez, A. E., Allende Prieto, C., Holtzman, J. A., et al. 2016, AJ, 151, 144, doi: 10.3847/0004-6256/151/6/144
Gelman, A., & Rubin, D. B. 1992, Statistical Science, 7, 457, doi: 10.1214/ss/1177011136
Gunn, J. E., Siegmund, W. A., Mannery, E. J., et al. 2006, AJ, 131, 2332, doi: 10.1086/500975
Hekker, S., Snellen, I. A. G., Aerts, C., et al. 2008, A&A, 480, 215, doi: 10.1051/0004-6361:20078321
Hogg, D. W., Myers, A. D., & Bovy, J. 2010, ApJ, 725, 2166, doi: 10.1088/0004-637X/725/2/2166
Holtzman, J. A., Hasselquist, S., Shetrone, M., et al. 2018, AJ, 156, 125, doi: 10.3847/1538-3881/aad4f9
Homan, M. D., & Gelman, A. 2014, J. Mach. Learn. Res., 15, 1593. http://dl.acm.org/citation.cfm?id=2627435.2638586
Hut, P., McMillan, S., Goodman, J., et al. 1992, PASP, 104, 981, doi: 10.1086/133085
Ivanova, N., Justham, S., Chen, X., et al. 2013, A&A Rv, 21, 59, doi: 10.1007/s00159-013-0059-2
Jayasinghe, T., Stanek, K. Z., Kochanek, C. S., et al. 2019, MNRAS, 485, 961, doi: 10.1093/mnras/stz444
Jeans, J. H. 1919, MNRAS, 79, 408, doi: 10.1093/mnras/79.6.408
Jenkins, J. S., Díaz, M., Jones, H. R. A., et al. 2015, MNRAS, 453, 1439, doi: 10.1093/mnras/stv1596
Jones, E., Oliphant, T., Peterson, P., et al. 2001–, SciPy: Open source scientific tools for Python. http://www.scipy.org/
Kipping, D. M. 2013, MNRAS, 434, L51, doi: 10.1093/mnrasl/slt075
Kollmeier, J. A., Zasowski, G., Rix, H.-W., et al. 2017, arXiv e-prints, arXiv:1711.03234. https://arxiv.org/abs/1711.03234
Kouwenhoven, M. B. N., & de Grijs, R. 2008, A&A, 480, 103, doi: 10.1051/0004-6361:20078897
Lindegren, L., Hernández, J., Bombrun, A., et al. 2018, A&A, 616, A2, doi: 10.1051/0004-6361/201832727
Majewski, S. R., Schiavon, R. P., Frinchaboy, P. M., et al. 2017, AJ, 154, 94, doi: 10.3847/1538-3881/aa784d
Meibom, S., & Mathieu, R. D. 2005, ApJ, 620, 970, doi: 10.1086/427082
Moe, M., & Di Stefano, R. 2017, ApJS, 230, 15, doi: 10.3847/1538-4365/aa6fb6
Moe, M., & Kratter, K. M. 2018, ApJ, 854, 44, doi: 10.3847/1538-4357/aaa6d2
Moe, M., Kratter, K. M., & Badenes, C. 2019, ApJ, 875, 61, doi: 10.3847/1538-4357/ab0d88
Nidever, D. L., Holtzman, J. A., Allende Prieto, C., et al. 2015, AJ, 150, 173, doi: 10.1088/0004-6256/150/6/173
Nocedal, J., & Wright, S. J. 2006, Numerical Optimization, 2nd edn. (New York, NY, USA: Springer)

Paxton, B., Bildsten, L., Dotter, A., et al. 2011, ApJS, 192, 3, doi: 10.1088/0067-0049/192/1/3
Paxton, B., Cantiello, M., Arras, P., et al. 2013, ApJS, 208, 4, doi: 10.1088/0067-0049/208/1/4
Paxton, B., Marchant, P., Schwab, J., et al. 2015, ApJS, 220, 15, doi: 10.1088/0067-0049/220/1/15
Pérez, F., & Granger, B. E. 2007, Computing in Science and Engineering, 9, 21, doi: 10.1109/MCSE.2007.53
Price-Whelan, A. 2019, adrn/hq: The version used to run on APOGEE DR16, dr16, Zenodo, doi: 10.5281/zenodo.3596084
Price-Whelan, A., Breivik, K., D'Orazio, D., et al. 2019, BAAS, 51, 206
Price-Whelan, A., & Hogg, D. W. 2019, adrn/thejoker v1.0, v1.0, Zenodo, doi: 10.5281/zenodo.3596088
Price-Whelan, A. M. 2017, The Journal of Open Source Software, 2, 388, doi: 10.21105/joss.00388
Price-Whelan, A. M., & Foreman-Mackey, D. 2017, The Journal of Open Source Software, 2, doi: 10.21105/joss.00357
Price-Whelan, A. M., & Goodman, J. 2018, ApJ, 867, 5, doi: 10.3847/1538-4357/aae264
Price-Whelan, A. M., Hogg, D. W., Foreman-Mackey, D., & Rix, H.-W. 2017, ApJ, 837, 20, doi: 10.3847/1538-4357/aa5e50
Price-Whelan, A. M., Hogg, D. W., Rix, H.-W., et al. 2018, AJ, 156, 18, doi: 10.3847/1538-3881/aac387
Queiroz, A. B. A., Anders, F., Chiappini, C., et al. 2019, arXiv e-prints, arXiv:1912.09778. https://arxiv.org/abs/1912.09778
Raghavan, D., McAlister, H. A., Henry, T. J., et al. 2010, ApJS, 190, 1, doi: 10.1088/0067-0049/190/1/1
Ricker, G. R., Winn, J. N., Vanderspek, R., et al. 2014, Society of Photo-Optical Instrumentation Engineers (SPIE) Conference Series, Vol. 9143, Transiting Exoplanet Survey Satellite (TESS), 914320, doi: 10.1117/12.2063489
Rix, H.-W., Ting, Y.-S., Sippel, A., et al. 2019, BAAS, 51, 104
Salvatier, J., Wiecki, T. V., & Fonnesbeck, C. 2016, PeerJ Computer Science, 2, e55, doi: 10.7717/peerj-cs.55
Shappee, B. J., Prieto, J. L., Grupe, D., et al. 2014, ApJ, 788, 48, doi: 10.1088/0004-637X/788/1/48
Sigurdsson, S., & Phinney, E. S. 1993, ApJ, 415, 631, doi: 10.1086/173190
Spencer, M. E., Mateo, M., Olszewski, E. W., et al. 2018, AJ, 156, 257, doi: 10.3847/1538-3881/aae3e4
Spencer, M. E., Mateo, M., Walker, M. G., et al. 2017, AJ, 153, 254, doi: 10.3847/1538-3881/aa6d51
Thompson, T. A., Kochanek, C. S., Stanek, K. Z., et al. 2019, Science, 366, 637, doi: 10.1126/science.aau4005
Troup, N. W., Nidever, D. L., De Lee, N., et al. 2016, AJ, 151, 85, doi: 10.3847/0004-6256/151/3/85
Walt, S. v. d., Colbert, S. C., & Varoquaux, G. 2011, Computing in Science and Engg., 13, 22, doi: 10.1109/MCSE.2011.37
Wilson, J. C., Hearty, F. R., Skrutskie, M. F., et al. 2019, PASP, 131, 055001, doi: 10.1088/1538-3873/ab0075
Zahn, J. P. 1977, A&A, 500, 121
Zamora, O., García-Hernández, D. A., Allende Prieto, C., et al. 2015, AJ, 149, 181, doi: 10.1088/0004-6256/149/6/181
Zasowski, G., Johnson, J. A., Frinchaboy, P. M., et al. 2013, AJ, 146, 81, doi: 10.1088/0004-6256/146/4/81

Zasowski, G., Cohen, R. E., Chojnowski, S. D., et al. 2017, AJ, 154, 198, doi: 10.3847/1538-3881/aa8df9

Zhao, G., Zhao, Y.-H., Chu, Y.-Q., Jing, Y.-P., & Deng, L.-C. 2012, Research in Astronomy and Astrophysics, 12, 723, doi: 10.1088/1674-4527/12/7/002